Colombian Trapiche Emeralds: Recent Advances in Understanding Their Formation

Isabella Pignatelli, Gaston Giuliani, Daniel Ohnenstetter, Giovanna Agrosì, Sandrine Mathieu, Christophe Morlot, and Yannick Branquet

Colombia is the traditional source of the world's finest emeralds, including the famed trapiche crystals, with their distinctive texture resembling a wheel with six spokes. This gemological curiosity, found exclusively in the black shales of the country's western emerald zone, is linked to the peculiar structural geology of the deposits. The study presents a review and update on Colombian trapiche emeralds, followed by a three-dimensional examination of the crystals combined with spectroscopic and chemical analyses. The proposed formation model incorporates the structural geology of the deposits with the formation of trapiche and non-trapiche emeralds. The fluid accumulation at the faults' tip in the black shales leads to maximum fluid overpressure and sudden decompression and formation of the emerald-bearing vein system. The authors show that trapiche emerald growth starts at the beginning of the decompression that is responsible for local supersaturation of the fluid. The hydrothermal fluid comes in contact with the black shale matrix, favoring the formation of emerald seed crystals. During the growth of these seeds, textural sector zoning occurs, sometimes associated with chemical sector zoning, along with displacement of the matrix. Displacement growth occurs because the emeralds continue their growth, pushing the matrix material away from the growing faces. An overgrowth, generally of gem quality, can form after decompression, surrounding the core, the arms, and the dendrites, restoring the emeralds' euhedral habit.

Colombian emeralds continue to set the standard as the finest and most spectacular crystals unearthed (Ringsrud, 2013). Unique mineralogical curiosities include the emerald gastropods extracted from the Matecaña mine in Gachalà (Vuillet et al., 2002) and the famous gem-trapiche emeralds (figure 1) such as the 80.61 ct Star of the Andes (Ward, 1993).

The past 25 years have seen major advances in our understanding of the formation of Colombian emeralds (Ottaway et al., 1994; Cheilletz et al., 1994), but the genesis of trapiche emerald remains unresolved despite analytical and geological advances. This type of emerald is very rare and has been recovered only occasionally, from just a few mines on the western side of the Eastern Cordillera Basin. Named after the Spanish word for the cogwheels used in sugar mills, these mineral curiosities are prized by collectors. The texture on a section perpendicular to the c-axis is characterized by a central core, six arms, and *dendrites* between the arms and around the core (figure 1). An overgrowth may also be present. The trapiche texture can be observed in other minerals, such as rubies, tourmalines, chiastolites, and garnets (box A). Without a link between field observation and mineralogical studies, there is still no consensus on the causes of the growth mechanism and texture acquisition, or on the geological conditions necessary for the formation of trapiche emerald.

This article provides an update on Colombian trapiche emerald, with complete historical, geological, mineralogical, gemological, and crystallographic background. The review opens debate on the key question of the geological conditions necessary for the formation of gem-quality trapiche material. The

See end of article for About the Authors and Acknowledgments.
Gems & Gemology, Vol. 51, No. 3, pp. 222–259,
http://dx.doi.org/10.5741/GEMS.51.3.222.

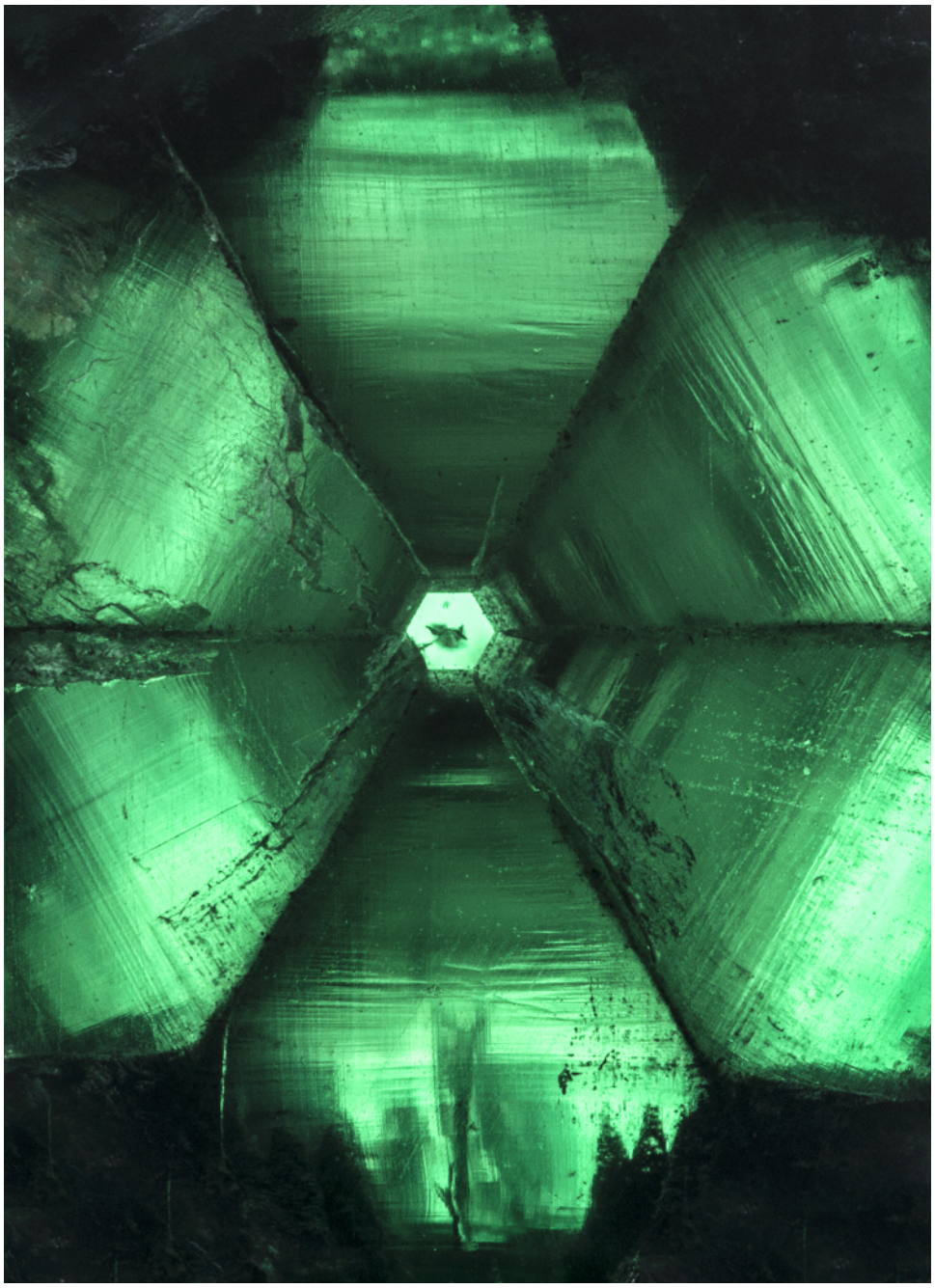

Figure 1. Looking down the crystal axis of a backlit 58.83 ct trapiche emerald from Peñas Blancas (also featured on the cover of this issue). Photo by Robert Weldon/GIA, courtesy of Jose Guillermo Ortiz, Colombian Emerald Co.

ongoing research into the mineralogy, chemical composition, and crystallography of trapiche emerald is connected with field expeditions conducted by French and Canadian research teams during the 1990s that proposed the hydrothermal sedimentary model now recognized by the scientific and exploration communities (Maya et al., 2004; Mantilla Figueroa et al., 2007). The scope is to propose a coherent mechanism for the formation of trapiche, linking it for the first time to the genetic model of Colombian emeralds. Colombia offers a unique case because other gem trapiches have not been studied intensively in connection with their geological setting. For the gemologist, this knowledge offers a better understanding of the mineralogy of trapiche emerald and a deeper appreciation of the complex geologic processes required to form such a peculiar mineral texture. Geologic terms that might be unfamiliar to the reader are defined in the glossary and italicized upon first mention within the text.

BOX A: TRAPICHE VS. TRAPICHE-LIKE MINERALS

Win (2005) distinguished three types of trapiche minerals as a function of their appearance due to coloring elements, other mineral inclusions, or intergrowth of the same mineral. Schmetzer et al. (2011) improved this distinction, defining only two groups: "trapiche" minerals and "trapiche-like" minerals (figure A-1).

Trapiche minerals are characterized by crystallographically equivalent growth sectors that are separated by more or less sharp boundaries of inclusions (figure A-1, left). The boundaries intersect in a central point or extend from the edge of a central core. Gems that belong to this group include emeralds from Colombia, corundum (e.g., Müllenmeister and Zang, 1995; Schmetzer et al., 1996, 1998; Sunagawa, 1999; Garnier et al., 2002a, 2002b), tourmalines (Hainschwang et al., 2007; Schmetzer et al., 2011), chiastolites (Rice and Mitchell, 1991; Rice, 1993), and garnets (Harker, 1950; Atherton and Brenchley, 1972; Wilbur and Ague, 2006).

We also mention two examples of non-Colombian trapiche emerald crystals, one from the Brazilian state of Goiás (DelRe, 1994) and the other from the Mananjary area in Madagascar (Johnson and Koivula, 1998). The Brazilian crystal showed fibrous arms and a tapered core. The specimen from Madagascar presented the spoke-like texture associated with Colombian emerald. The core was limited to a center point, while the dendrites contained black material. These two gems refer more to trapiche than trapiche-like emeralds, but they cannot be compared with Colombian samples because their geological formation is unknown.

Two other features observed in trapiche crystals should be mentioned: symmetry and inclusions of organic matter. Trapiche minerals are always characterized by high symmetry: cubic for garnet, hexagonal for emerald, and trigonal for corundum and tourmaline. The only exception is chiastolite, which belongs to the orthorhombic system but is pseudotetragonal ($a \approx b$). The symmetry affects the number of arms and dendrites in the trapiche texture, as well as the directions where the dendrites develop. Because high symmetry implies that a certain number of directions are equivalent, the positions of the dendrites can be predicted taking into account the crystal system. For example, in emerald there are six dendrites respectively along the positive and negative sides of the a-axis, whereas in chiastolite the four dendrites are along the a- and b-axes.

To the best of our knowledge, no trapiche texture has been reported in minerals with low symmetry (orthorhombic, monoclinic, or triclinic), even though the development of dendrites on the corners of minerals with euhedral morphology such as olivine is already known (Faure et al., 2003, 2007). This suggests that at least two of the three basic vectors *a*, *b*, and *c* have to be equal (or, in the case of chiastolite, nearly equal) to obtain the trapiche texture, and thus the role of symmetry cannot be neglected.

The presence of transformed organic matter or graphite is observed in trapiche minerals formed in different geological environments—for instance, metamorphic deposits such as ruby (Garnier et al., 2002a,b), chiastolite, garnet (Rice and Mitchell, 1991), and tourmaline (Schmetzer et al., 2011). The role of carbonaceous materials in trapiche formation was raised by Rice and Mitchell (1991) and Rice (1993), referring to Burton (1986), who stated that graphite can control the fluid composition and dictate the mechanism and timing of mineral growth.

In trapiche-like minerals, the texture is caused by the distribution of color-inducing elements or of inclusions in alternating portions of the crystal (figure A-1, right). This is the case with sapphire (Koivula et al., 1994; Khotchanin et al., 2010; Kiefert, 2012), quartz (Win, 2005), and aquamarine (Koivula, 2008; Befi, 2012). Cordierite-indialite intergrowths also show a trapiche-like texture, as described by Rakovan et al. (2006).

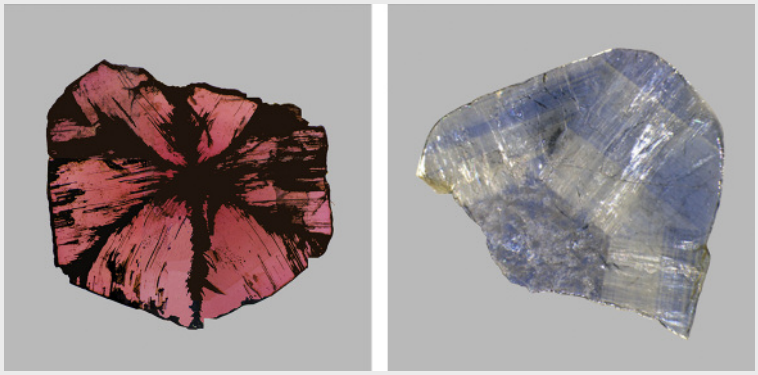

Figure A-1. Trapiche vs. trapiche-like corundum. Left: Trapiche ruby originating from marble in Mong Hsu (Myanmar). The trapiche texture is characterized by dendrites and arms, though the specimen lacks a central core. Photo by V. Garnier. Right: A pinacoidal section of a trapiche-like blue sapphire from the Changle alkali basalt (China), showing a hexagonal core and outer zones with a fine oscillatory zoning. Photo by G. Giuliani.

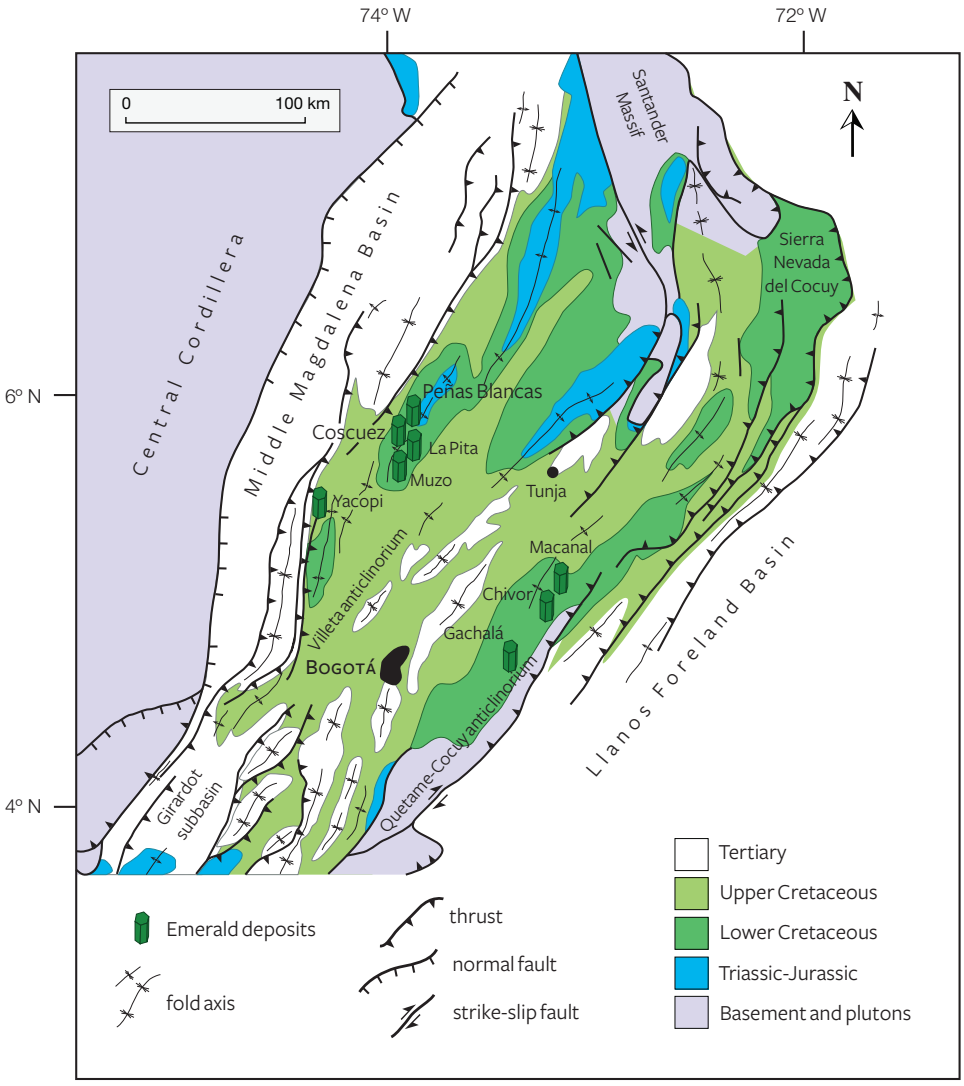

Figure 2. Simplified geological map of the Eastern Cordillera Basin in Colombia. The emerald deposits are hosted by Lower Cretaceous sedimentary rocks forming two mineralized zones located on the eastern and western border of the basin, respectively. The western border contains the mining districts of La Glorieta–Yacopi, Muzo, Coscuez, La Pita, and Peñas Blancas, while Gachalá, Chivor, and Macanal lie on the eastern border.

GEOLOGY OF COLOMBIAN EMERALDS: AN UPDATE

Geological Setting. Located in the Eastern Cordillera Basin, the Colombian emerald deposits consist of two belts. On the western side lie the mining districts of Muzo, Coscuez, La Pita, Peñas Blancas, and La Glorieta–Yacopi. On the eastern side are Chivor, Gachalá, and Macanal (figure 2). The Eastern Cordillera is a slightly folded belt *overthrusting* the Llanos Foreland Basin to the east and the Middle Magdalena Basin to the west. The belt resulted from the tectonic inversion at the Middle Miocene (15 Ma), during the Andean tectonic phase, of the central part of the *subsiding marine basin*. The major part of the Eastern Cordillera is formed by thick folded and faulted Mesozoic sedimentary series. Emerald mineralization is hosted in the Neocomian series of the Lower Cretaceous (135–116 Ma). The sediments are characterized by a succession of beds of sandstones, limestones, *black shales*, and *evaporites*.

The deposits from the eastern belt are contained in the Berriasian limestone–black shale horizon (135–130 Ma) of the Guavio Formation, which is overlain by siliceous black shales of the Valanginian Macanal Formation (130–122 Ma). In the Chivor mining district, the host rocks comprise the Guavio Formation shale sequences that contain intercalations of limestone lenses and gypsum beds, as suggested by phantom nodules, mesh and chevron textures, and *coquina limestone* grading to black shales intercalated with *olistostromes* (Branquet, 1999).

The deposits from the western belt are contained in the black shales and intercalated *dolomitic limestones* of Valanginian-Hauterivian age (130–116 Ma)

corresponding to the Rosablanca and Paja Formations. The lithostratigraphic column, from bottom to top, is formed by dolomitic limestones from the Rosablanca Formation, calcareous carbon-rich black shales from the Hauterivian that are the main emerald-bearing horizon, siliceous black shales (Hauterivian), and mudstones of the Barremian-Aptian Paja Formation (116–108 Ma).

The ages of emerald formation were obtained indirectly by argon-argon dating of syngenetic green muscovite. From this analysis, the first date was 65 Ma in the eastern zone, at the Cretaceous-Tertiary boundary when the dinosaurs disappeared (Cheilletz et al., 1997). The second date was between 38 and 32 Ma in the western zone, at the time of the Eocene-Oligocene boundary (Cheilletz et al., 1994).

Emerald Mineralization. In the two mineralized belts, emerald-bearing veins are spatially associated with stratiform *breccias* and white or black *albitites*, the latter resulting from the albitization of the black shales. The veins are parallel, *en echelon*, or conjugate arrays forming two successive stages of extensional vein systems (Cheilletz and Giuliani, 1996). Stage 1 is accompanied by a bedding-parallel vein system filled by fibrous calcite, pyrite, and green muscovite. It is associated with the formation of *décollement* fault planes that focused the hydrothermal fluids and induced formation of albite and calcite in the black shales. The sodium *metasomatism* led to leaching of major (Si, Al, K, Ti, Mg), trace (Ba, Be, Cr, V), and rare-earth elements from the enclosing black shales (Beus and Mineev, 1972; Beus, 1979; Ottaway, 1991; Giuliani et al., 1993; Mantilla Figueroa et al., 2007). Stage 2 is characterized by faulting and folding associated with *extensional vein* sets and *hydraulic breccias* filled with calcite and dolomite, pyrite, muscovite, albite, bitumen, and the precipitation in *drusy cavities* of fluorite, apatite, parisite, dolomite, emerald, and quartz (Hall, 1993).

In Brief

- Trapiche emeralds are found in the black shales of a few Colombian mines, in the western belt of the Eastern Cordillera Basin. They are characterized by a texture, visible perpendicular to the crystal's c-axis, that usually consists of a central core, six arms, and dendrites between the arms and around the core.
- While trapiche emeralds are formed from the same fluid as gem-quality Colombian emeralds, their texture results from a complex growth history characterized by fluid pressure variations.
- The formation of trapiche emeralds is controlled by the structural geology of the deposits and by the crystal's symmetry, which determines the number and the development of growth sectors.

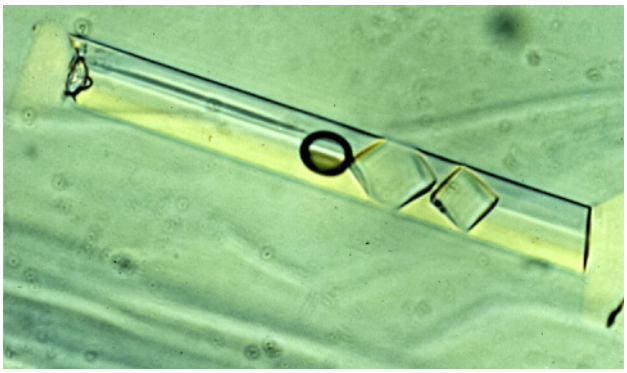

Figure 3. Primary multiphase fluid inclusion trapped in an emerald from El Oriente mine in the Chivor district. The cavity, 180 µm long, contains (from right to left) two cubes of sodium chloride (halite), a rounded gas bubble, and two minute calcite crystals, with salt water occupying 75 vol.% of the cavity. The cavities usually contain only one cube of salt, but sometimes two or three cubes crystallize during fluid cooling. Photo by Hervé Conge.

The Colombian emerald deposits were previously thought to be associated with mafic or granitic intrusions (Beus and Mineev, 1972; Ulloa, 1980). Detailed geochemical studies undertaken in the 1990s led to a hydrothermal model involving the circulation of hot *basinal brines* (Kozlowski et al., 1988; Ottaway, 1991; Giuliani et al., 1991; 1992; 1995; 2000; Cheilletz et al., 1994; Ottaway et al., 1994; Banks et al., 2000; Mantilla Figueroa et al., 2007). The fluids trapped by emerald are three-phase or multiphase fluid inclusions (figure 3) characterized by the presence of a cube (or occasionally two or three cubes) of halite (NaCl). At room temperature, the fluid inclusion cavities contain 75 vol.% salty water—in other words, a brine (liquid H_2O, 10 vol.% gas corresponding to the vapor bubble, and 15 vol.% halite *daughter mineral*). The mineralizing solutions are basinal brines that interacted with evaporites. The H_2O-NaCl-CO_2-(Ca-K-Mg-Fe-Li-SO_4) fluids (Banks et al., 2000) are NaCl-saturated [~40 wt.% equivalent NaCl] and were trapped at approximately 300–330°C (Roedder, 1984; Ottaway et al., 1994). The CO_2 densities of fluid inclusions range from 0.02 to 0.25 g/cm^3 and indicate that emerald crystallized under variable fluid pressure. The increase of CO_2 pressure caused fluid *overpressure* in

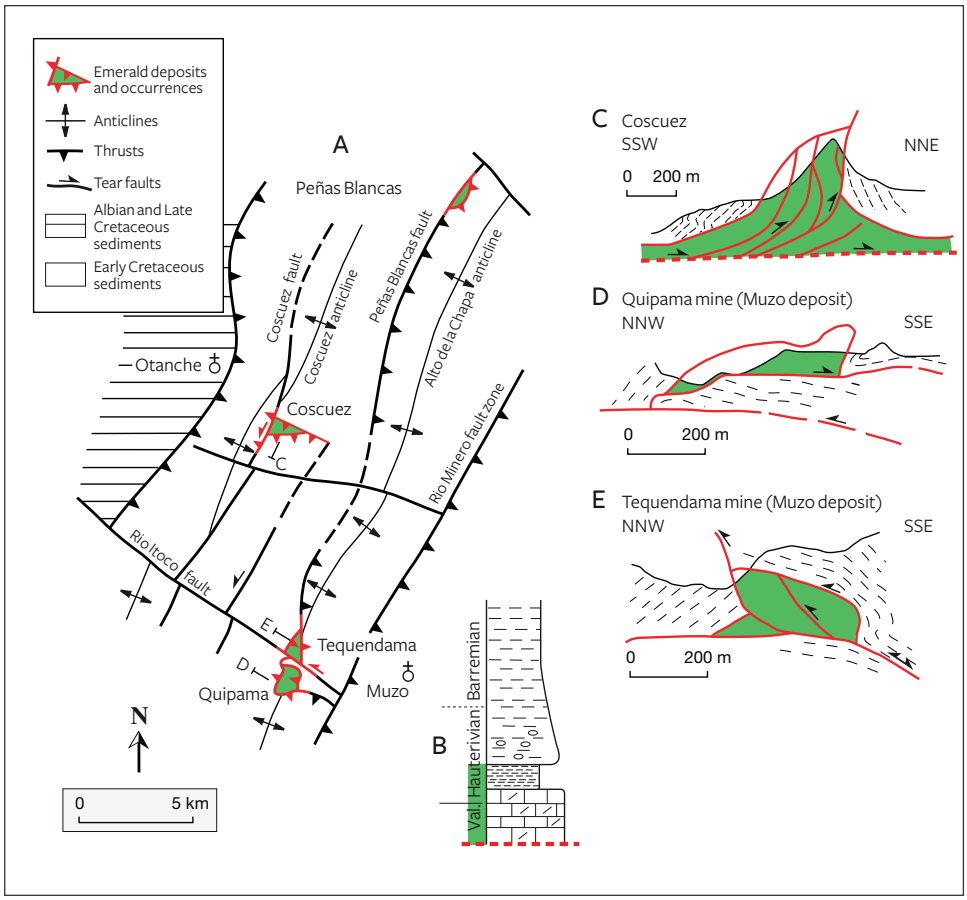

Figure 4. Tectonic settings of Colombia's western emerald zone (modified from Branquet et al., 1999a). A: Structural location map of the emerald deposits and the regional structures, from Rodriguez and Ulloa (1994). B: Lithostratigraphic column of the emerald-bearing formations. From bottom to top: lowermost Cretaceous rocks, Valanginian-Hauterivian dolomitic limestone, Hauterivian calcareous carbon-rich black shale, Hauterivian siliceous black shale, and Barremian-Aptian mudstones. The red dotted line represents the décollement zone. C through E: Emerald deposits of Coscuez, Quipama, and Tequendama mines (Muzo district).

the black shales and consequent fracturing and brecciation (Ottaway et al., 1994). The high-salinity brines interacted with calcareous shales rich with black organic matter. Sulfate ions (SO_4^{2-}) in minerals of evaporitic origin were reduced by organic matter in the black shale to form hydrogen sulfide (H_2S) and bicarbonate (HCO_3^-), which are responsible for the crystallization of pyrite and carbonates, respectively, with bitumen in the veins being derived from the organic matter.

The *thermal reduction of sulfate* by organic matter, at 300°C, released the chromium, vanadium, and beryllium in the black shale, which in turn enabled emerald formation (Ottaway et al., 1994; Cheilletz et al., 1994).

Structural Setting and Type of Mineralization. Detailed structural mapping and geometric analysis suggest that structural controls on mineralization are drastically different between the western and eastern sides of the Colombian emerald belt (Branquet, 1999; Branquet et al., 1999a,b). Muzo and Coscuez are characterized by compressive structures formed along *tear faults* (figure 4), whereas the eastern emerald deposits such as Chivor present extensional structures branched on a brecciated evaporitic level that acted as a local, gravity-driven *detachment* (Branquet et al., 2015). These tectonic structures are synchronous with the circulation of the hydrothermal fluids and emerald deposition.

On the western side, the deposits measure about 100 meters across and display numerous folds, *thrusts* (Pogue, 1916; Scheibe, 1926), and tear faults (Laumonier et al., 1996). At Muzo, thrusts are evidenced by the presence of calcareous black shales over siliceous black shales. All the tectonic contacts are marked by centimeter- to meter-thick hydrothermal breccias called "cenicero" (ashtray) by the local miners (Scheibe, 1926). These white or red breccias outline the thrust planes, which are associated with intense hydraulic fracturing due to overpressured fluids (Giuliani et al., 1990; Ottaway et al., 1994; Branquet et al., 1999b). The breccias are *cataclasites*, with clasts of calcareous black shales and white albitite within a carbonate-albite-pyrite cement. Multistage brecciation corresponds to successive fault-fluid flow pulses, and dilatant sites result from *shear*-fracturing synchronous to the thrust-fault propagation. Each

Figure 5. Geological map of the Muzo mines, with the height of each mining site reported in bold. Modified from Barriga Villalba (1948).

pulse is associated with (1) emerald-bearing banded carbonate vein-like structures present throughout the breccia; (2) emerald-bearing thrust-associated carbonate veins occurring in the wall rocks formed of calcareous black shales, called "cama" by the local miners; (3) emerald-bearing carbonate dykes escaping from the breccia zone and crosscutting the wall rocks; (4) en echelon sigmoidal *tension gashes*; and (5) *drag folds* indicating shearing in the roof of the breccia zones. All these tectonic structures are associated with fluid circulation in the calcareous carbon-rich black shale, inducing intense albitization, carbonatization, and pyritization. The siliceous black shales, called "cambiado" by the local miners, have no mineralization (Oppenheim, 1948).

From a geological study in 1914–1915, Pogue (1916) described the trapiche texture but did not provide the precise location of the source. Scheibe (1926, 1933) identified the disseminations of trapiche emerald in the black shales from the Banco Amarillo. ("Banco" refers to a mineralized level, and "amarillo" is Spanish for yellow; here the yellowish color is due to pyrite alteration.) The geological map of Banco de la Republica (Barriga Villalba, 1948) indicates that Banco Amarillo was formed by the breccia zone, albitites, and the emerald-bearing veins (figure 5). The geological map by Laumonier et al. (1996) shows that a preserved remnant of the Banco Amarillo level (figure 6) is located under the administration building of the Muzo mine and corresponds to a *klippe* of the calcareous black shale that overthrust the siliceous black shale. Since 1948, this emerald-bearing formation has been exploited further to the southwest up to the Gallinazo, Zincho, and Malvinas mining workings (compare figures 5 and 6). Furthermore, Ottaway (1991) reported that "more recently trapiche have been found in the shale adjacent to larger bodies of Cenicero."

In the Coscuez deposit, the lithostratigraphic column is formed, from bottom to top (Branquet, 1999), by *dolomitic limestone* forming the peak of El Reten, calcareous carbon-rich black shale, and siliceous black shale. The folds and thrusts were guided by the Coscuez tear fault, which acted as a vertical conduit for the mineralizing fluids developed in the calcareous carbon-rich black shale (figure 4B). Breccia, formed by opening of dilatant sites related to fluid pressures and hydrothermal replacement, are similar to those described for the Muzo deposit (Branquet et al., 1999b). Trapiche emeralds have been found at Coscuez but have never been described by geologists.

In conclusion, the deposits on the western side formed as the consequence of a compressive phase characterized by folding and thrusting along tear faults at the time of the Eocene-Oligocene boundary. These complex structures imply the existence of a basal regional décollement fault at a level of evaporites (Branquet et al., 1999b). The fluid circulation is linked to the thrust-fault propagation.

On the eastern side, the mines are scattered along a regional white-brecciated level that contains emer-

ald (Branquet, 1999; Branquet et al., 1999a, 2015). The brecciated level in the Chivor area, more than 10 km long and 1–10 meters thick, is stratiform (i.e., parallel to the sedimentary strata) and largely made of hydrothermal breccia formed by fragments of the hanging wall (carbonated black shale, limestone, and whitish albitite), cemented by carbonates and pyrite. Its formation is related to the dissolution of an evaporitic horizon. All the mineralized structures are branched from the brecciated level. In the Chivor mines, emerald is located in centimeter- to decimeter-thick carbonate- and pyrite-bearing *listric faults*, meter-wide extensional fractures injected with hydrothermal breccia, and extensional sets of fractures in the calcareous carbon-rich black shales of the Macanal Formation. According to a member of the family that has owned the Chivor mines for many years, trapiche emeralds have never been found there or anywhere else in the eastern zone of the Eastern Cordillera (D. Oswaldo, pers. comm., 2014). Nevertheless, Nassau and Jackson (1970) claimed to have studied a thousand trapiche emeralds from these mines, and their article raised the question of Chivor origin. In conclusion, the brecciated level, the hydrothermal fluid circulation and emerald formation occurred at the same time, at the Cretaceous-Tertiary boundary (~65 Ma), during an extensional tectonic event linked to evaporite dissolution and driven by gravity (Branquet et al., 1999a, 2015).

Therefore, trapiche emeralds are only found in the deposits on the western side (Muzo, Coscuez, and Peñas Blancas) of the Eastern Cordillera Basin. The trapiche emerald–bearing deposits are formed along thrust and fault planes associated with fluid circulations, intense hydraulic fracturing of the enclosing black shales forming breccias, and carbonate veins. Trapiche and non-trapiche emeralds are associated with these compressive structures.

EMERALD: STRUCTURE AND HABIT

Emerald is a gem variety of beryl, a cyclosilicate with the ideal formula $Be_3Al_2Si_6O_{18}$. Its structure is characterized by six-membered rings of silica tetrahedra lying in planes parallel to (0001). The rings are linked laterally and vertically by two kinds of coordination polyhedra, both distorted: BeO_4 tetrahedra and AlO_6 octahedra (figure 7). The stacking of these six-membered rings forms large open channels parallel to the c-axis with nonuniform diameter, consisting of cavities with a diameter around 5.1 Å separated by bottlenecks with a diameter of about 2.8 Å. The channels may be filled by alkali ions (such as Na^+,

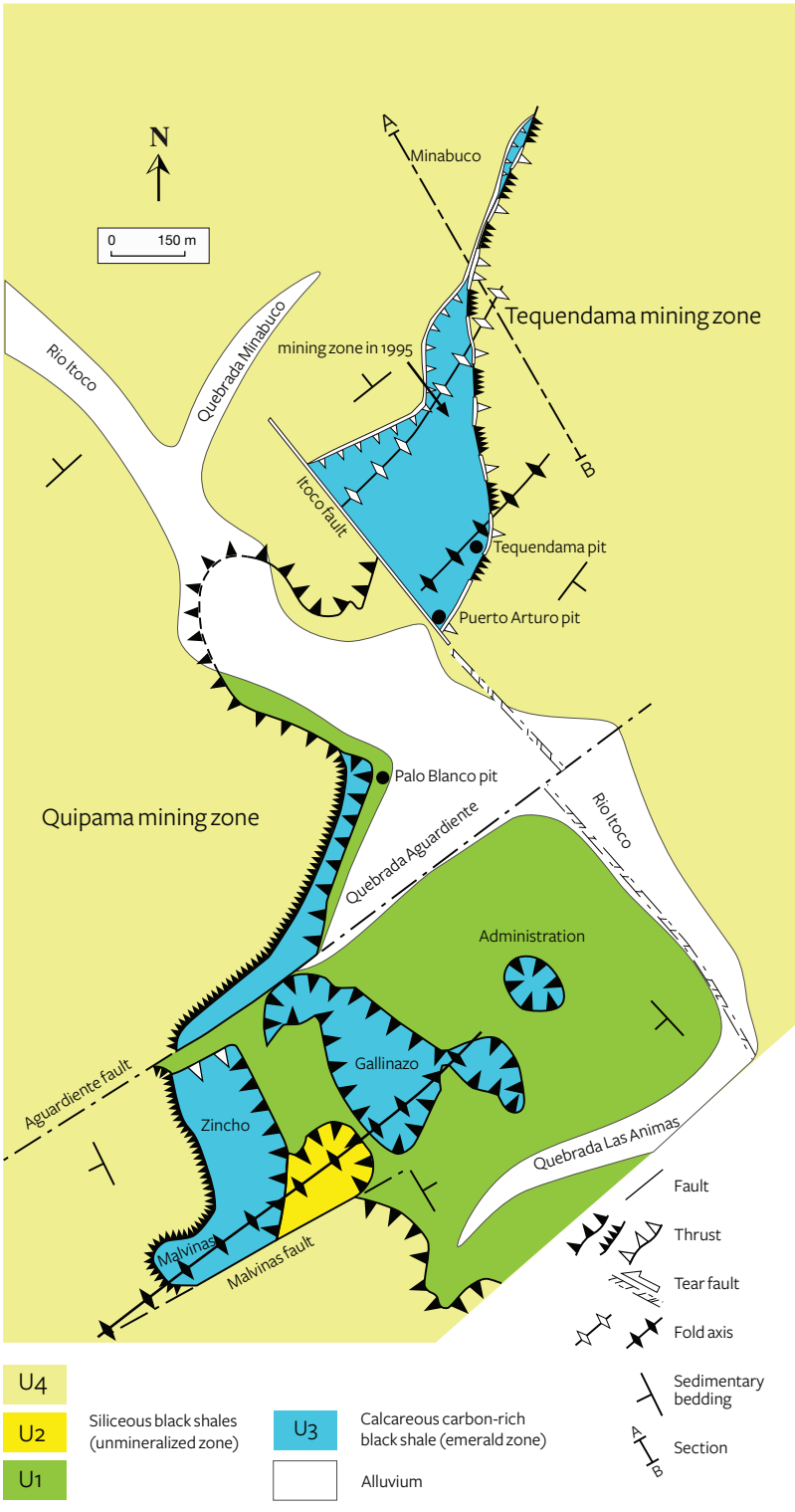

Figure 6. Geological map of the Muzo mines, where U1 through U4 represent the different tectonic units. U1, U2, and U4 are composed of barren siliceous black shales, while U3 consists of the emerald-bearing calcareous carbon-rich black shale. Modified from Laumonier et al. (1996).

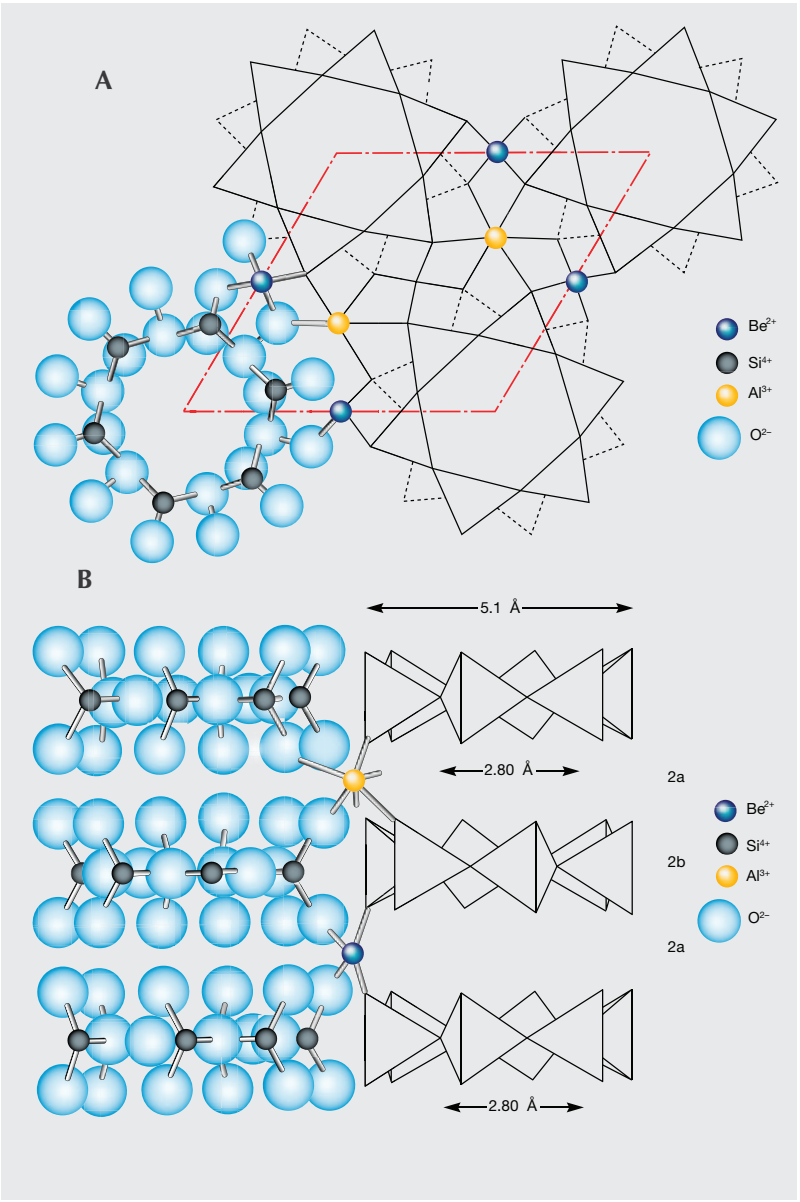

Figure 7. The structure of beryl, as seen in an apical view (A) and a lateral view (B). In the apical view, hexagonal silicate rings stacked parallel to the c-axis (normal to the drawing) are held together by Al^{3+} (octahedral site) and Be^{2+} (tetrahedral site). The lateral view, which is perpendicular to the apical view, shows the hexagonal silicate rings and the bottleneck (2b site) and open-cage (2a site) structures. From Charoy (1998).

Li^{+}, K^{+}, Rb^{+}, and Cs^{+}) that are needed to balance the positive charges when cation substitutions occur in the structure. For example, Be^{2+} can be substituted with Li^{+} (Aurisicchio et al., 1988), whereas Al^{3+} is generally replaced by Fe^{2+}, (Mg^{2+}, Mn^{2+}), Cr^{3+}, V^{3+}, or Ti^{4+} (Groat et al., 2014). Variable amounts of neutral H_2O and CO_2 molecules (Wood and Nassau, 1968) and noble gases such as argon, helium (Damon and Kulp, 1958), xenon, and neon (Giuliani et al., 2005) are also normally present in the channels.

Emerald is defined by Schwarz and Schmetzer (2002) as "the yellowish green, green or bluish green beryl which reveals distinct chromium and/or vanadium absorption bands in the red and blue violet ranges of their absorption spectra." The quantitative ranges of the Cr and V substitutions are between 25 ppm (Wood and Nassau, 1968) and 3.4 wt.% (Andrianjakavah et al., 2009) for Cr_2O_3, and between 34 ppm (Zwaan et al., 2012) and 2.44 wt.% (Rondeau et al., 2008) for V_2O_3. Emerald crystallizes in the hexagonal system with cell parameters a = 9.218(2) Å, c = 9.197(2) Å, $\alpha = \beta = 90°$, and $\gamma = 120°$, and its *space group* is *P6/mcc* (Artioli et al., 1993). Its typical habit is prismatic (figure 8), characterized by eight faces and their corresponding growth sectors: six $\{10\bar{1}0\}$ first-order prismatic faces and two *pinacoidal* {0001} faces. Small additional $\{10\bar{1}2\}$ and $\{11\bar{2}2\}$ faces may also be present in some crystals.

TRAPICHE COLOMBIAN EMERALD: A REVIEW

Colombian trapiche emeralds were first described by the French mineralogist Emile Bertrand (1879), in a meeting at the Société Géologique de France, in which he presented "curious crystals of emerald… from Muso, New Granada." All 40 samples displayed a nearly colorless hexagonal center surrounded by a green portion. The latter is described as having striations parallel to the sides of the central hexagon and with "modifications" in the directions tangential to the sides of the hexagon. No further information was added about the composition or the nature of the "modifications." Bergt (1899) described a cut trapiche emerald from Muzo received by the geologist Stübel in 1868. Similar emeralds were reported by Codazzi (1915) in an accurate listing of Muzo's minerals. These emeralds were reported to have a cyclic twinning, as observed in aragonite. This contradicted the optical observations of Pogue (1916), who stated that these emeralds were not twinned. According to Pogue, the presence of re-entrant angles was due to "the effect of solution, the disposition of carbonaceous inclusions and the crystallizing forces, as shown also, for example, in chiastolite." It is worth noting that the Pogue study contained the first mention of inclusions of carbonaceous matter in the emeralds, "arranged in a six-rayed centering about a tapering hexagonal core."

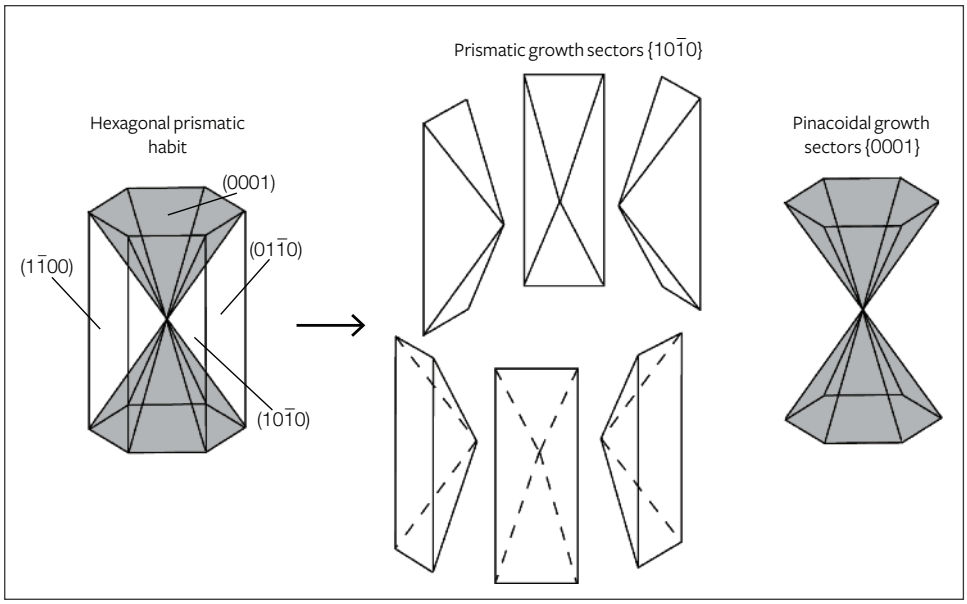

Figure 8. The habit of emerald crystals, characterized by eight main faces and their corresponding growth sectors: six {10$\bar{1}$0} first-order prismatic faces and two pinacoidal {0001} faces. Adapted from Rakovan et al. (2006).

During a geological study of Muzo in 1914–15, Scheibe (1926, 1933) collected several emeralds from the Banco Amarillo in the calcareous carbon-rich black shales of the Lower Cretaceous (again, see figure 5). These emeralds appeared very different from those usually found in the veins, and for this reason they were analyzed in detail by Bernauer (1933). Different morphologies were observed, as shown in figure 9: euhedral hexagonal prismatic emeralds (figure 9A), but also crystals with signs of corrosion along the edges of the prism (figures 9B to 9E). The emeralds showed dark, fibrous inclusions between the prismatic edges, starting from the middle of the crystal and enlarging toward the prism's corners. The inclusions, which seemed to be emphasized by the corrosion, were composed of quartz, muscovite, carbonates, pyrite, and a dark carbonaceous matter (probably with an organic or bituminous origin), sometimes with biotite and kaolin. Multiphase inclusions with liquid, vapor, and solid phases were also observed. The core of the emeralds had the shape of two opposite hexagonal pyramids with their vertices located in the middle of the crystal. Sometimes these pyramids were so unevenly developed that the core resembled a column. The core was richer in inclusions, some of them more darkish to black, than the rest of the crystal. In fact, it can be surrounded by the dark inclusions (figure 9B), entirely composed of the dark inclusions (figure 9D), or formed by several parallel crystals separated by dark inclusions (figure 9C). In some emeralds the inclusions can be whitish instead of dark, due to the presence of albite and kaolin.

Although Bernauer (1933) suggested that these trapiche emeralds were due to cyclic twinning as in cordierite, chrysoberyl, aragonite, or other minerals, he emphasized that the growth rates in the different crystallographic directions played an important role in the incorporation of the dark inclusions and, thus, in the formation of these emeralds. Nevertheless,

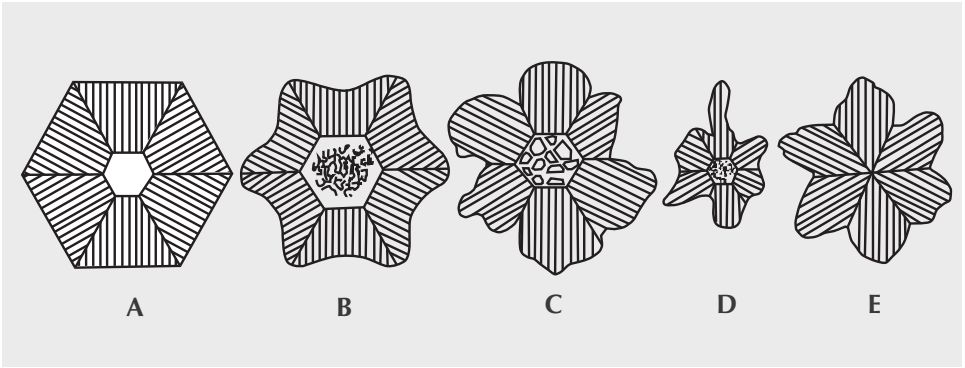

Figure 9. Different morphologies of trapiche emeralds from the Muzo mine, described by Bernauer (1933). A: Euhedral hexagonal prismatic crystals with no sign of corrosion. B through E: Crystals showing different degrees of corrosion along the prism's edges.

Barriga Villalba (1948) described the unusual trapiche emeralds from Muzo as aragonite-type twins of scientific interest but no gemological value. Studying the mineralogical features of Muzo emeralds, Barriga Villalba (1948) pointed out the special aspects of the core in crystals of different sizes. The gem core was formed by pyramidal and hexagonal cones presenting a three-dimensional geometric shape that tapered smoothly from the pinacoid to the vertex. These gem cones, sometimes of high quality, were extracted from the emerald crystal.

The 1960s saw further studies on Colombian trapiche emerald, with the discovery in 1963 of new material in the Peñas Blancas mines (Tripp and Hernandez, 1970). In 1964, McKague introduced the term "trapiche" to name the unusual Colombian emerald whose crystal habit was similar to the cane-crushing gears used by farmers. According to McKague, trapiche emerald was characterized by four morphological elements:

1. A central deep green hexagonal prism tapered toward one end and without inclusions
2. Six trapezoidal-shaped prisms extending from the $\{10\bar{1}0\}$ faces of the central prism and containing opaque inclusions
3. A colorless fine-grained beryl occurring between and within the six trapezoidal prisms but also in the central prism, with opaque minerals (probably altered in limonite) observed on and between the beryl grains
4. An overgrowth separated from the six prisms by scattered patches of opaque inclusions

McKague was the first to propose a genetic model for the formation of trapiche emeralds. In this model, the central prism formed first. A change in pressure, temperature, and chemical composition or a combination of these parameters caused the formation of the trapezoidal prisms. A further change in the system led to the overgrowth's formation. At the end, a more drastic change occurred and the trapezoidal prisms were partially converted into fine-grained beryl at the intersections of the $\{10\bar{1}0\}$ faces.

In 1967, Leiper examined unusual trapiche emeralds reportedly from the Chivor mine. The core and the six arms branching from it were emerald of good quality, while the material between the arms was a whitish-greenish beryl. This low-quality material was compared to the fine-grained beryl described by McKague, usually called "moralla" by the local miners.

In 1968, Schiffman analyzed trapiche crystals to identify them as natural or synthetic. The presence of channels, three-phase fluid inclusions, and solids (organic matter, possibly graphite, as well as quartz and albite) confirmed their natural origin. Chaudhari (1969) described the emeralds with the unusual gear-shaped pattern as composite crystals made of two distinct entities: a hexagonal pale green core and a dark green overgrowth on the prism faces. Around the core, the sectors were separated by a very fine-grained clay-like matrix (containing abundant quartz). Some of the sectors were irregular and formed by *stringers* that grew from the core to the faces. Small stringers of emeralds at 60° angles to each other in the matrix were also described, but only in the gaps between the sectors. According to Chaudhari, the sawtooth contact between the matrix and the sectors with the stringers indicated that several changes occurred in the chemical and physical conditions during trapiche growth.

Nassau and Jackson (1970) marked a real advance in the understanding of trapiche formation after Bernauer (1933). Nevertheless, this work raised a questionable point on the origin of trapiche material. The authors claimed to have studied a thousand trapiche emeralds from Chivor and only two from Muzo. Between 1963 and 1970, trapiche emeralds came only from the Peñas Blancas and Muzo mines. Leiper (1967) had not specified the provenance of his samples, leading to a series of misunderstandings in subsequent bibliographic citations. But Leiper's photos of the trapiche emeralds resembled those presented by Tripp and Hernandez (1970) for the Peñas Blancas mine. Samples from Peñas Blancas were given to Leiper by M. Anderton, manager of the Chivor emerald mine, and this is probably the source of the confusion over the origin of the stones studied by Nassau and Jackson. Finally, Sinkankas and Read (1985) clarified the provenance of the trapiche emeralds described by Nassau and Jackson, asserting that they were from Peñas Blancas.

Examinations of cross-sections of single crystals have shown considerable variation in the structure of trapiche emerald; see figure 10. Nassau and Jackson (1970) used the terms "core," "arms," and "two-phase region." The hexagonal core may or may not be present (figure 10C), and it is usually of good-quality emerald, but it is possible to find samples with one end as in figure 10B and the other as in figure 10C. The core usually has a taper, as previously noted by Pogue (1916), Barriga Villalba (1948), and McKague (1964). The emerald formed on the prism faces of the core are named "arms," because their

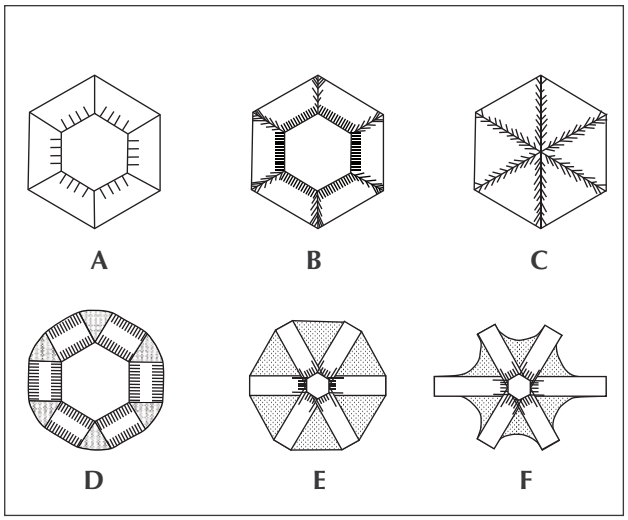

Figure 10. Schematic cross-sections of different trapiche emeralds described by Nassau and Jackson (1970).

shape is not always trapezoidal (as described in previous works). Moreover, the arms may be asymmetrical (figure 10F). The material observed between the arms as well as between the core and the arms can be white/gray or dark. The white to gray material is formed by a mixture of emerald and albite, while the dark material is carbonaceous, even if it contains albite. Trapiche emeralds with a core completely composed of this dark material have also been reported.

Nassau and Jackson (1970) rejected the hypothesis of twinning to explain trapiche formation. They proposed two mechanisms, one for the samples purportedly from Chivor and one for the Muzo samples. In the "Chivor" samples, the central core formed first, followed by beryl growth on its prism faces. Simultaneously, a dendritic growth of both beryl and albite under *eutectic* conditions occurred at the corners of the central core. The presence of beryl-albite can be also related to an abrupt increase in the growth rate of the arms. In fact, this favors the trapping of the foreign phase (albite in this case) at the interface between the growing "arms." According to the authors, all Chivor samples are grown "in the same time, in the same or similar environments, in a relatively small region." To explain the formation of Muzo samples, they suggested instead an abrupt decrease in the growth rate of the arms and/or an increased concentration of carbonaceous material in the growth medium.

In 1971, O'Donoghue synthesized the work of Nassau and Jackson (1970) and remarked that the whitish gray or dark inclusions are not randomly distributed but follow the "hexagonal axis," i.e., the <100> directions in the hexagonal system (a-axis).

Two decades later, Van der Giessen (1994) reported several Colombian trapiches, among them a special sample with two hexagonal cores surrounded by eight trapezoidal sectors (figure 11). This sample seems to be a rare case of contact twinning in trapiche emeralds. According to the author, the formation of the trapiche is related to sector zoning. This peculiar example is perhaps closer to the unusual double-trapiche emeralds from Muzo reported by Hsu (2013), which consist of twelve fine arms intersecting in a central point. These samples are described as "composed of two six-ray stars shifted slightly from each other," though one might think they are twinned.

Ohnenstetter et al. (1998) studied Colombian trapiche emeralds from Muzo, Coscuez, and Peñas Blancas. The cores were colorless, and the trapezoidal growth sectors were colored with vivid green overgrowths. Cathodoluminescence underlined the chemical zoning due to variations of vanadium (V) and chromium (Cr). The first published microprobe data on trapiche emerald confirmed that the green zones were V-rich ($0.5 < V_2O_3 < 0.79$ wt.%) and relatively Cr-poor ($0.35 < Cr_2O_3 < 0.39$ wt.%). The colorless hexagonal prism was a Cr- and V-free beryl. Scanning electron microscope observation of sections perpendicular to the c-axis showed streaks along the trapezoidal growth sectors and a feathery aspect to the inclusions in the arms of the crystals. The arms were formed mainly of albite and beryl, with some apatite and pyrite. The authors thought that trapiche emeralds resulted from a

Figure 11. Schematic cross-section of an exceptional trapiche emerald examined by Van der Giessen (1994). The emerald is characterized by two hexagonal cores surrounded by eight trapezoidal sectors.

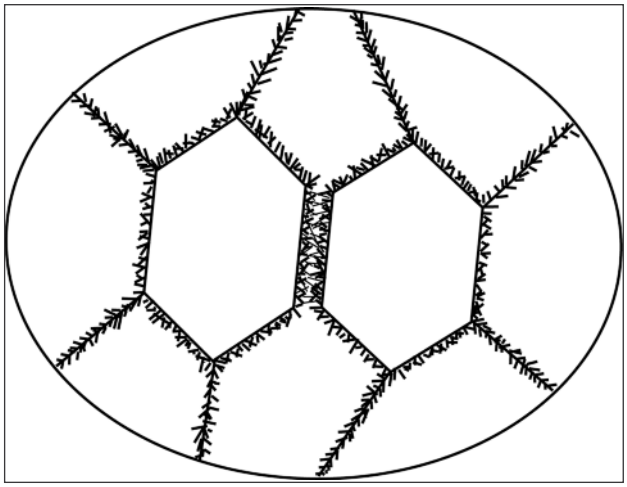

BOX B: Crystal Nucleation, Growth, and Texture

Sunagawa (1987, 1999) proposed that crystal morphology depends on the degree of supersaturation (also called undercooling) that conditioned the driving force and explained the evolution of crystal habit by changes in growth mechanism. Figure B-1 presents the driving force versus the growth rate anisotropy. The driving force is characterized by two critical points (X and Y) where the predominant growth mechanism changes: spiral growth for a low driving force, two-dimensional nucleation growth (2DNG) for an intermediate driving force, and an adhesive growth mechanism for a high driving force. The expected morphologies change from polyhedral to hopper or skeletal and then to fractal, spherulitic, and dendritic.

Crystals demonstrating rapid growth textures are found in many rock types and geological environments: pillow basalts (Bryan, 1972), granites and pegmatites (London, 2008), magmatic olivine (Faure et al., 2003), chiastolites and garnets in metamorphic environments (Burton, 1986; Rice, 1993), metasomatic tourmalines (Byerly and Palmer, 1991), and finally in trapiche emeralds and rubies (Sunagawa et al., 1999).

As stated by Nassau and Jackson (1970) for Colombian emerald, trapiche starts to grow as a beryl in the core, and then as coeval albite and beryl in the dendrites and stringers in the arms. Based on this mineralogical evidence with the simultaneous growth of both albite and beryl, the growth of trapiche emerald could be interpreted as a eutectic binary system (Nassau and Jackson, 1970), though such a system of albite and beryl has not been investigated up to now. In the same way, Sunagawa et al. (1999) also considered the dendritic morphology and mineral composition (corundum and carbonate) of trapiche ruby that was formed under eutectic growth conditions.

Despite the fact that Colombian trapiche emerald is related to basinal fluid circulation, the association of albite-beryl in a H_2O-NaCl ±(CO_2) fluid seems to be similar to paragenesis in low-temperature H_2O-saturated pegmatites. In such a magmatic system, supersaturation is the driving force of the crystallization, and so the rate of nucleation and growth is driven by supersaturation in the solution. In a binary diagram of temperature and composition, the displacement of the liquidus (the temperature above which a magma is molten) may occur in response to changes in pressure, temperature, or composition (London, 2008). A decrease in pressure such as a drop in the H_2O fluid pressure in an H_2O-saturated melt will provoke a decompression, providing the driving force of crystallization with dendritic textures (London, 2008). In the case of Colombian emerald, the decompression phenomena by a drop of H_2O (and CO_2) fluid pressure at the tip of the faults induced a huge supersaturation that provided the driving force to initiate crystallization of the dendrites of trapiche emerald composed of albite and emerald. The predominance of albite over emerald in the dendrites indicates a great undercooling that promoted the crystallization first of albite and then emerald.

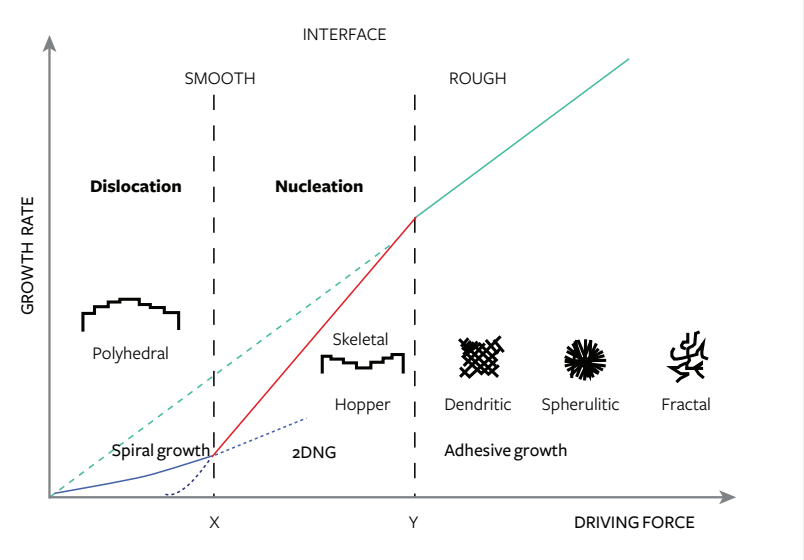

Figure B-1. This diagram shows the three types of crystal growth mechanisms (Sunagawa, 1999): spiral growth (blue curve), two-dimensional nucleation growth (2DNG; red curve), and adhesive growth (green curve). The nature of the interfaces is classified as either rough or smooth. The growth rates are determined by the state of the interfaces, which are classified as either rough or smooth. The increasing intensity of the driving force is presented between the critical points X and Y, where nucleation occurred. A rough interface is expected above Y and smooth interface below X, where dislocation occurred.

rapid and skeletal growth, complicated by interactions between the hydrothermal fluids and the black shales.

Sunagawa et al. (1999) compared the formation of trapiche emeralds to trapiche rubies in light of crystal

growth mechanisms, presenting evidence of many parallels (box B). Two main differences were pointed out: the typical absence of the core in rubies, and the dissimilar geological settings. However, the formation mechanism seems to be the same for both minerals: if a core is present, it is formed at first by *layer-by-layer* growth under small driving force conditions. When the driving force increases, a *dendritic* multiphase growth occurs around the core. Then, a decrease of the driving force leads to layer-by-layer growth and the formation of the ruby or emerald sectors. The contemporaneousness of the two last stages is not ruled out by Sunagawa et al. (1999).

In the past decade and a half, the main features of Colombian trapiche emeralds have been revisited in an exhaustive work by Hochleitner (2002); Giuliani et al. (2002) added that they are only found on the western side of the Eastern Cordillera Basin as material "disseminated in black shales or albitized black shales near emerald-bearing veins." Garnier et al. (2002) compared the geological setting of trapiche rubies from Mong Hsu in Myanmar with that of Colombian trapiche emeralds; the results underscored the differences in deposit type, fluid circulation, and *P-T* conditions of formation. Hainschwang et al. (2007) and Schmetzer et al. (2011) compared Zambian trapiche tourmalines to Colombian trapiche emeralds. Their studies suggested similar formation, depending on the growth rates of different sectors of the crystals. Both minerals contain dark carbonaceous inclusions along the a-axis, but the main visual difference is the tourmaline's three-sectored core due to the trigonal system of crystallization (space group *R*3*m*).

NEW SCIENTIFIC ADVANCES ON THE COLOMBIAN TRAPICHE EMERALDS

Material and Methods. The twelve trapiche emeralds examined in this study were provided in 1998 by Omar Bustos Santana, manager of Sociedad Esmeralda Ltda. (figure 12; table 1). The samples came from three Colombian mines: Coscuez (figures 12A–12C), Peñas Blancas (figure 12D), and Muzo (figures 12E–12L). These samples were stubby and small; their diameters varied from approximately 4.0 mm to 1.2 cm, generally with lengths of a few millimeters, with the exception of one sample approximately 1.1 cm long (figure 12I). The habit of the trapiche emeralds could not be well defined owing to the presence of a whitish or dark material; nevertheless, the pinacoidal {0001} faces and first-order prism $\{10\bar{1}0\}$ faces were recognizable in many of them. The color varied from one sample to another, but also within different portions of the same sample (from pale to deep green). The samples were prepared either as polished sections for electron microprobe analysis (EPMA), scanning electron microscopy (SEM), and cathodoluminescence analysis, or cut and polished on both sides to a thickness of 150–200 µm for microscopic examination. The main source and features of the crystals, and the different analytic methods applied for each trapiche emerald, are reported in table 1.

EPMA was performed at the University of Lorraine in Nancy's SCMEM laboratory on a fully automated Cameca SX100. The detection limits for trace elements in mass percentage were 715 ppm for Mn, 500 for Na and Si, 300 for Mg and Al, 110 for K, 40 for Ti, and 100 for V, Cr, and Fe. Data reduction was performed with the PAP program (Pouchou and Pichoir, 1991). Chemical formulas of emerald were calculated on the basis of 3 Be and 18 O apfu. BeO was determined by stoichiometry and H_2O by the equation derived from experimental data (Giuliani et al., 1997): H_2O (in wt.%) = (0.84958 × Na_2O (in wt.%) + 0.8373).

Cathodoluminescence (CL) and back-scattered electron (BSE) images were recorded at the SCMEM laboratory using an FEG JEOL J7600F SEM with an accelerating voltage of 15 kV and a beam current of 10 to 20 nA for the X-ray analysis and 2 nA for the CL images. This SEM is equipped with a Gatan MonoCL2 system with three diodes measuring the intensity of light in different wavelength regions, so the observed colors correspond to those of the visible spectra. CL images were also obtained under a Technosyn cold CL device, where the electrons are generated by an electric discharge between two electrodes under low gas pressure.

Trapiche emeralds were investigated by X-ray diffraction topography (XRDT) at the University of Bari, Italy, to obtain the spatial distribution and full characterization of the crystal defects in the whole sample volume (Lang, 1959). Topographic images were taken in transmission geometry using a conventional Lang camera (Rigaku ME110ED) with monochromatic $MoK\alpha_1$ radiation (λ = 0.709 Å) and a micro-focus X-ray tube. To minimize the X-ray absorption according to the Beer-Lambert law, the optimum kinematic diffraction condition $\mu t \approx 1$ (μ = linear absorption coefficient; t = crystal thickness) must be followed. Diffraction contrast was recorded on Kodak SR photographic film. The structural defects were characterized by applying the extinction criteria to their diffraction contrasts, ac-

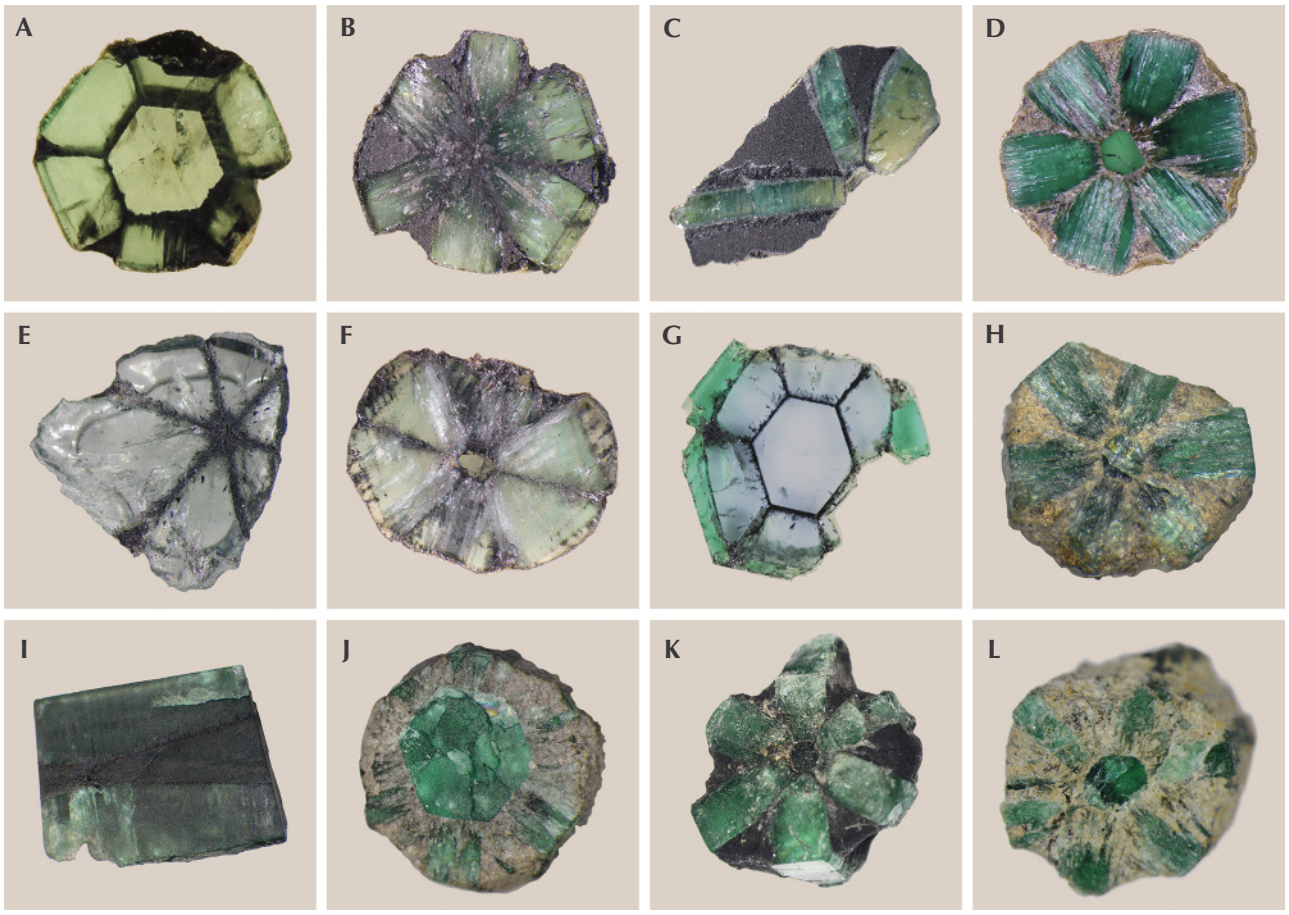

Figure 12. The Colombian trapiche emeralds studied in this work originate from the Coscuez (A–C), Peñas Blancas (D), and Muzo (E–L) mines. The sample sizes are reported in table 1. Shown are samples T2 (A), T3 (B), T4 (C), T5 (D), T6 (E), T7 (F), T8 (G), T9 (H), T10 (I), T11 (J), T12 (K), and T13 (L).

cording to kinematic and dynamic X-ray diffraction theories (Authier and Zarka, 1994).

X-ray computed tomography (CT) scanning is a non-destructive technique used in this study to reveal 3D interior details of trapiche emeralds. Images were made with a Phoenix Nanotom S scanner, using a resolution of 3.4 µm/voxel and a nanofocus X-ray tube tension value of 100 kV. Virtual cross-sections from all axes were extracted from the volume to observe the physical structure (e.g., inclusions and porosity) and to detect the presence of phases with different densities in the samples. The Nanotom scanner produces files with voxel (3D pixel) resolutions between 30.0 and 0.6 µm as a function of sample size. X-ray computed tomography has already been used for geoscience applications (Breeding et al., 2010; Tsuchiyama et al., 2005; Cnudde and Boone, 2013; Jia et al., 2014) but never previously for colored gems, because the X-ray exposure can strongly modify their colors. Here the technique was applied for the first time to analyze emeralds with satisfactory results and above all without color modification.

RESULTS

In figure 13A, two sections of a trapiche emerald, perpendicular and parallel to the c-axis, are illustrated schematically: one can distinguish the central core, the arms, the dendrites, and the overgrowth. It is worth noting that the trapiche emeralds are more developed perpendicular to the c-axis rather than along the c-axis. For this reason, it is rare to observe a section parallel to the c-axis, such as the example shown in figure 12I. Such sections are usually not available for scientific study, as trapiches are cut as cabochons that display their particular texture for jewelry.

The spatial relationships between the core, arms, and dendrites are visible in three perpendicular sections obtained by X-ray computed tomography (figure 14). Each aspect of the trapiche texture is described in detail below.

TABLE 1. Features and properties of the 12 trapiche emeralds investigated in this study.

Locality	Sample	Geometric pattern	Diameter (mm)	Section c-axis	Trapiche matrix	Composition (wt.%)		Solid inclusions	Microscopy	SEM	EPMA	XRDT	CT	CL
						(V_2O_3)	(Cr_2O_3)							
Coscuez	T2	Hexagonal crystal with core, arms, dendrites and small overgrowth	8	⊥	None	c: 0.13–0.15	0.00–0.04	Ab, Qtz, Brl, Ank, Dol	✓	✓	✓	✓		✓
						d: 0.16–0.20	0.02–0.03							
						a: 0.22–0.62	0.02–0.03							
						og: 0.62–0.90	0.05–0.90							
Coscuez	T3	Center, arms	6	⊥	AbBS			Ab, Dol, Brl, Cal, Qtz, Fap, Fe(O,OH), Ank, Py	✓	✓				
Coscuez	T4	Small core, arms, dendrites	Arm up to 10 mm	⊥	AbBS	c: 0.12–0.14	0.12–0.14	Ab, Cal, Brl, Tur, Rt, Mca, Fap, Po, Zrn, Dol, Kln	✓	✓	✓			✓
						d: 0.20–0.30	0.18–0.19							
						a: 0.20–0.30	0.15–0.20							
Peñas Blancas	T5	Hexagonal green core with green arms, dendrites	4	⊥	AbBS + clays	c: 0.68–0.72	0.30–0.40	Kln, Fe(O,OH), Ab, Rt, Brl, Zrn, Po, Cal, Dol, Fap, Mca	✓	✓	✓			✓
						d: 1.17	0.68							
						a: 0.90–1.16	0.0–0.90							
Muzo	T6	Center, asymmetric arms	Arm up to 3.5 mm	⊥	None				✓			✓		
Muzo	T7	Small core, arms, small overgrowth	10	⊥	None			Mca, Kln, Tur, Dol, Cal, Ank, Rt, Fe(O,OH), Qtz, Fl, Fap, Ab, Py	✓	✓				
Muzo	T8	Hexagonal crystal with hexagonal core and deep green overgrowth	10	⊥	None Clays in fractures	c: 0.02–0.03	0.00–0.02	Ab, Qtz, Mca, Rt, Dol, Brl	✓	✓	✓	✓		✓
						a: 0.02–0.06	0.00–0.06							
						og: 0.62–0.64	0.31–0.72							
Muzo	T9	Hexagonal green core and green arms	5	⊥	AbBS + clays			Brl, Mnz, Qtz, Pt, Fap, Ab, Mca, Rt, Fe(O,OH), Po	✓	✓			✓	
Muzo	T10	Bipyramidal core, arms	10	∥	None	c: 0.15–0.26	0.02–0.12	Ab, Kln, Fap	✓	✓	✓			
						a: 0.15–0.23	0.02–0.09							
Muzo	T11	Large green core, small arms	8, with core ~3 mm	⊥	AbBS + clays	c: 0.59–0.75	0.49–0.62	Brl, Qtz, Rt, Ab, Kln, Dol, Py	✓	✓	✓			✓
						d: 0.02–1.12	0.02–0.99							
						a: 0.91–1.09	0.73–0.89							
Muzo	T12	Small hexagonal core, arms	12	⊥	AbBS									
Muzo	T13	Core, arms	5	⊥	Ab									

c = core; d = dendrite; a = arm; og = overgrowth; AbBS = albitized black shale, Ab = albite; Cal = calcite; Qtz = quartz; Brl = beryl (emerald); Ank = ankerite; Dol = dolomite; Fap = F-apatite; Py = pyrite; Fe(O,OH) = iron oxides and hydroxides; Tur = tourmaline; Rt = rutile; Mca = muscovite; Po = pyrrhotite; Zrn = zircon; Kln = kaolinite; Fl = fluorite; Mnz = monazite; ∥ = section parallel to crystal's c-axis; ⊥ = section perpendicular to crystal's c-axis.

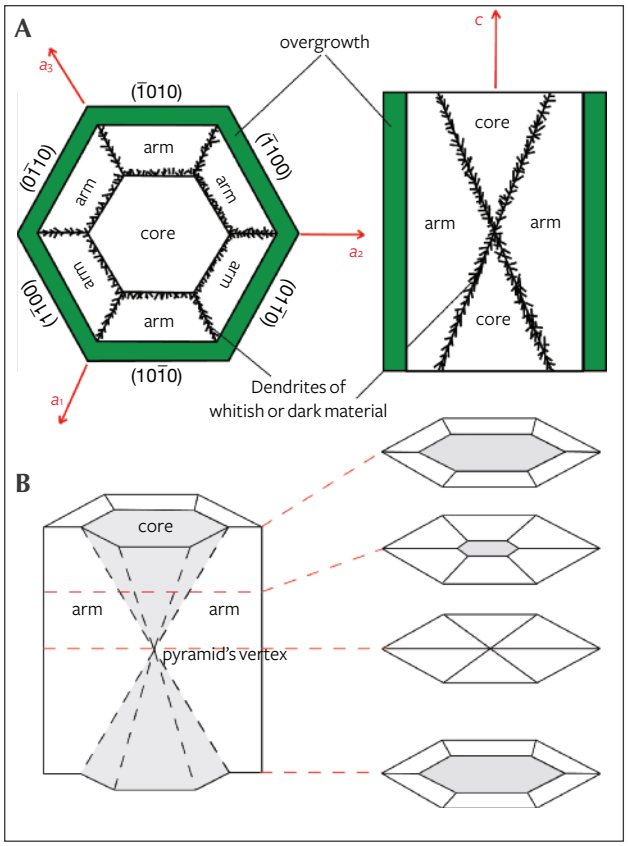

Figure 13. A: Schematic diagrams of trapiche emerald sections, perpendicular to the c-axis (top left) and parallel to it (top right). The sections show trapiche emerald's central core, arms, dendrites, and overgrowth zones. B: Aspect and variations of the core, which has a hexagonal bipyramidal shape. Its size varies as a function of the sections perpendicular to the c-axis: largest if the section is cut at the base of the pyramid, smallest near the pyramid's vertex.

Core. The central core may or may not be present in a trapiche emerald. The core is bounded by pinacoidal faces [0001] (see figures 12A, 12D, 12G, 12J, and 12L) and has the shape of two opposite hexagonal pyramids (figures 12I and 13) corresponding to the pinacoidal growth sectors. The presence and the size of the core depend on the position of the cross-section along the bipyramidal shape, as illustrated in figure 13B. If the trapiche's growth is homogeneous in both positive and negative directions of the c-axis, the two hexagonal pyramids will develop similarly. If the growth is inhomogeneous (due to limited space in the growth medium, for example), one pyramid will be more developed than the other, as in figure 12I. Moreover, in the sections perpendicular to the c-axis, the core is largest if the section is cut at the base of the pyramid, and smallest near

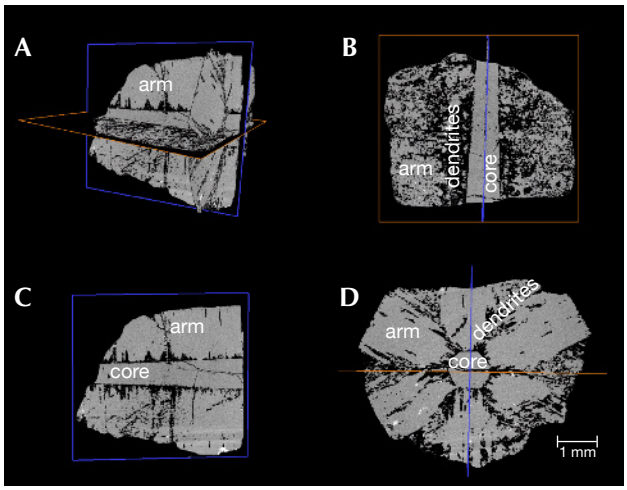

Figure 14. X-ray computed tomography images showing the spatial relationships between the core, arms, and dendrites in a trapiche emerald from Muzo.

the pyramid's vertex (figure 13B). This is confirmed by X-ray computed tomography: Figure 15A shows that the size of the core decreases from the top to the

Figure 15. X-ray computed tomography images of a trapiche emerald from Muzo. A: The size of the core decreases from the top toward the bottom of the crystal. B: The dendrites around the core develop laterally and penetrate into the arms. C: The spatial distribution and morphology of solid inclusions in the sample. D: The elevated porosity (in blue) of the whole sample in a section perpendicular to the c-axis.

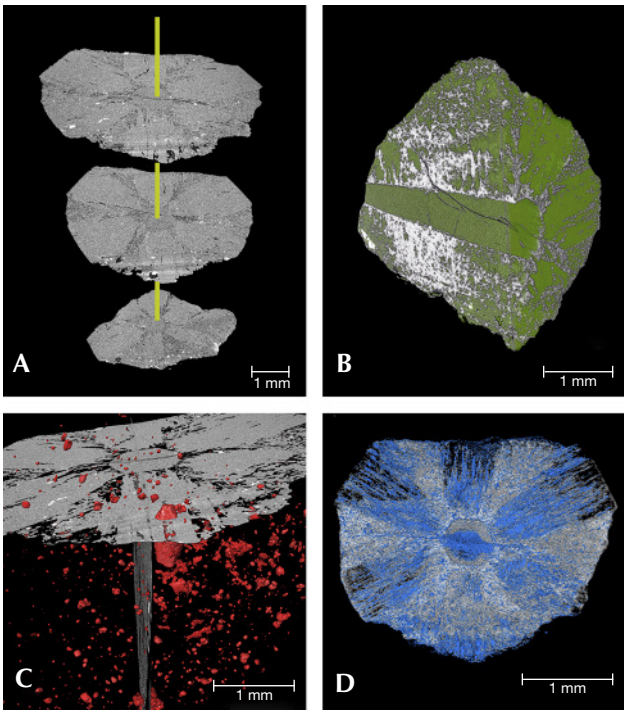

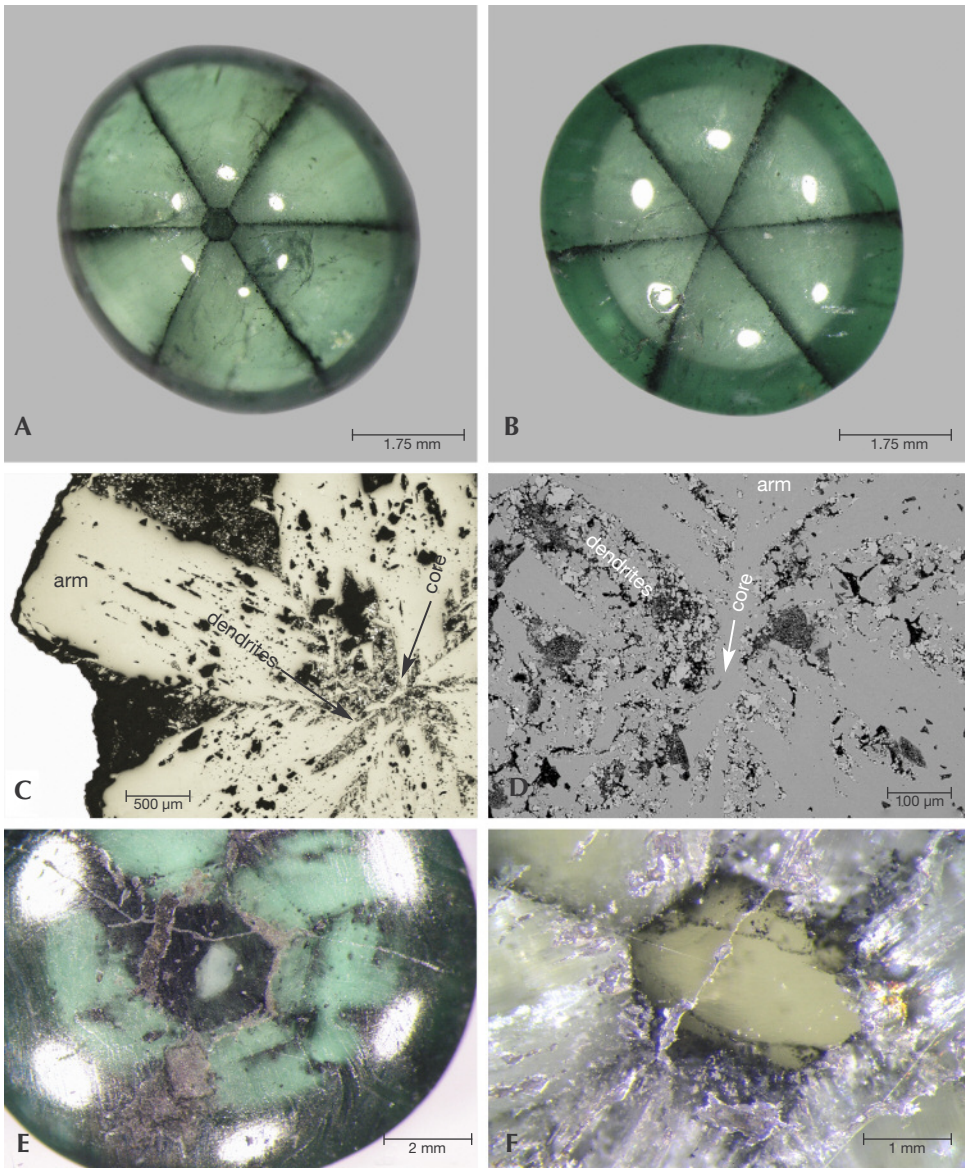

Figure 16. Core images of several trapiche emeralds. Samples showing the upper part of the cabochon cut with the hexagonal core (A), and with only a central point (B); optical (C) and SEM (D) images of a sample with no core, the dendrites and arms crossing in the central point; an example of a hexagonal dark core (E); signs of fracturing and dissolution in a core, attesting to a complex growth history (F).

bottom of the trapiche. When a section is cut between the vertices of two opposite pyramids, the core is absent and the arms and dendrites intersect in a central point, as in figures 12B, 12E, 16C, and 16D. This explains why some trapiche samples show a hexagonal core on one end (figure 16A) but no core on the other end (figure 16B). The color of the core can vary from very light to deep green, reflecting different quantities of the chromophores V^{3+} and Cr^{3+} (see the "Trace-Element Analysis" section below).

The core is surrounded by dendrites that can also replace it completely or partially, as described by Bernauer (1933). The replacement gives the core a dark aspect, as shown in figure 16E. The dendrites around the core develop laterally and penetrate into the arms, as demonstrated by the density contrast in the tomographic images (figures 14 and 15B).

Optical observations of the sections perpendicular to the c-axis under cross-polarized light confirm that the core cannot be completely extinct, but a kind of wavy extinction, as in quartz, is made visible by turning the stage of the microscope. It follows that the core may be plastically deformed during or after its formation. This particular optical feature was mentioned by Bernauer (1933), who wrote of "listas onduladas," and Chaudhari (1969), who described "a sort of grating structure" in the core.

Signs of dissolution are observed in the core of two samples. For example, figures 17A and 17B show that the core's edges are not straight, due to

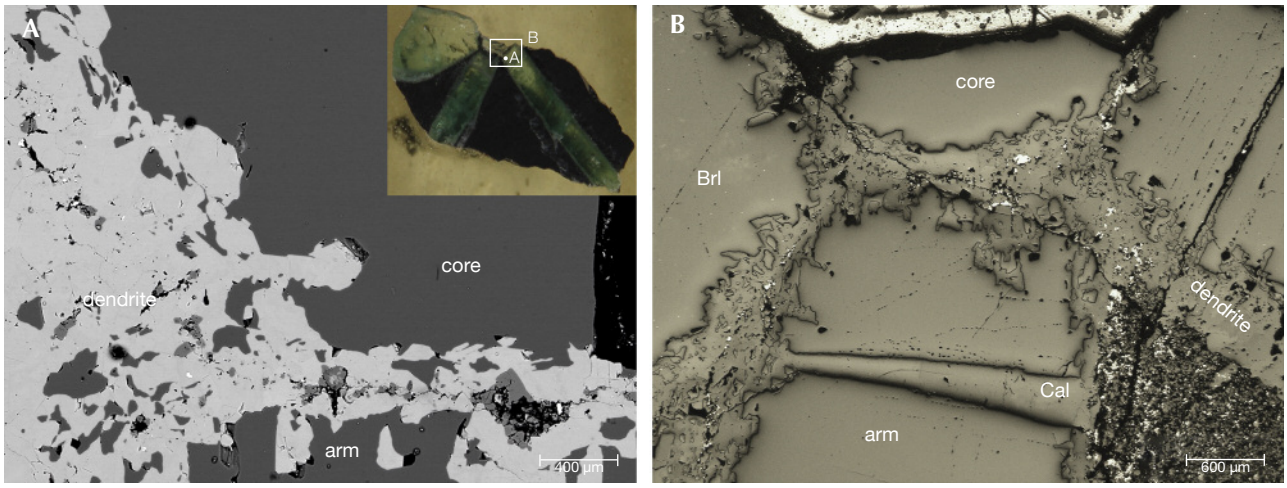

Figure 17. A: An SEM image of the spatial relationship between the core, dendrites, and arms in the sample from figure 12C. The inset shows the whole sample, along with the locations of images A and B. The wavy contact between the core and the dendrites indicates a previous dissolution of the core by the fluids. The dendrites are formed mainly by calcite and albite sometimes associated with beryl. B: A microscopic image of the dendrites and the arms of emerald (Brl), which formed simultaneously, though the arms were affected by dissolution and fracturing (see the aspect of the core and arms). The microscopic image shows that the fracture crosscutting the arm is filled by calcite (Cal) and ± albite associated with tiny beryl crystals (around ten microns).

etching, and are partially covered by the arms. In figure 16F, dissolution also occurred during the core's complex growth history. During its formation, the core underwent a deformational event marked by two main fractures coeval with the dendrites' development. The fractures are filled by the same minerals found in the dendrites: albite, pyrite, quartz, carbonates, fluorite, and *phyllosilicates*. Some of the fractures are filled by fluid inclusions, indicating fluid circulation and consequent dissolution of the edges and corners of the core. The effects of dissolution are marked by the modification of the core's shape from hexagonal to oval, and by the irregular etched borders. During a second stage, core

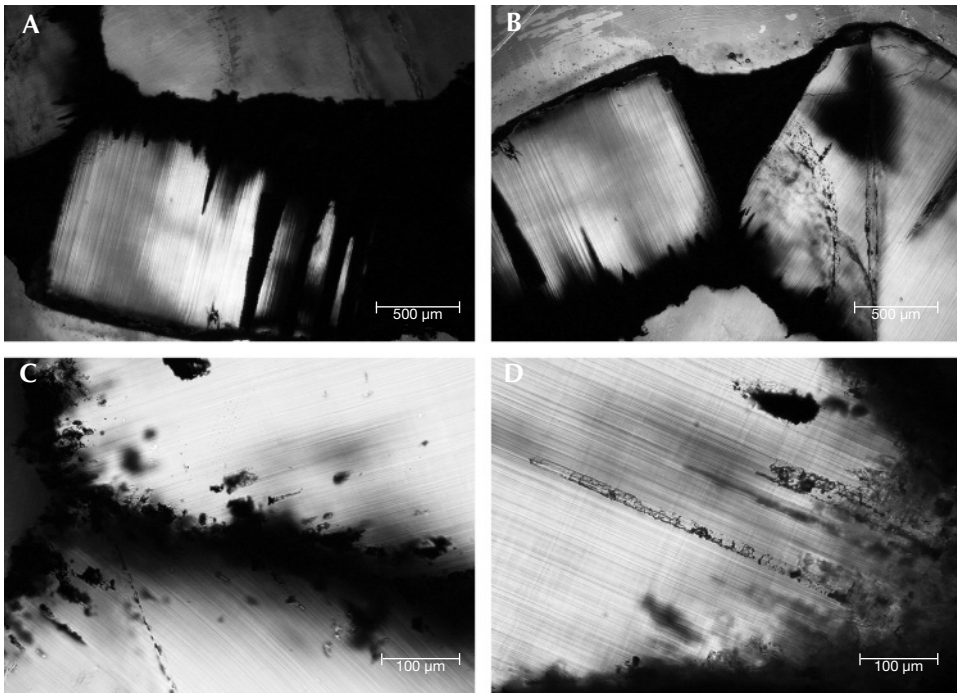

Figure 18. Optical images of growth arms in trapiche emeralds. A and B: The arms are characterized by bundles of straight dislocations perpendicular to the {10$\bar{1}$0} faces. C: Direction of propagation of the dislocations in two adjacent growth sectors. Along these dislocation zones and at the contact of the dendrites, the crystals trap solids and cavities of fluid inclusions. D: Primary fluid inclusion trails are parallel to the dislocations.

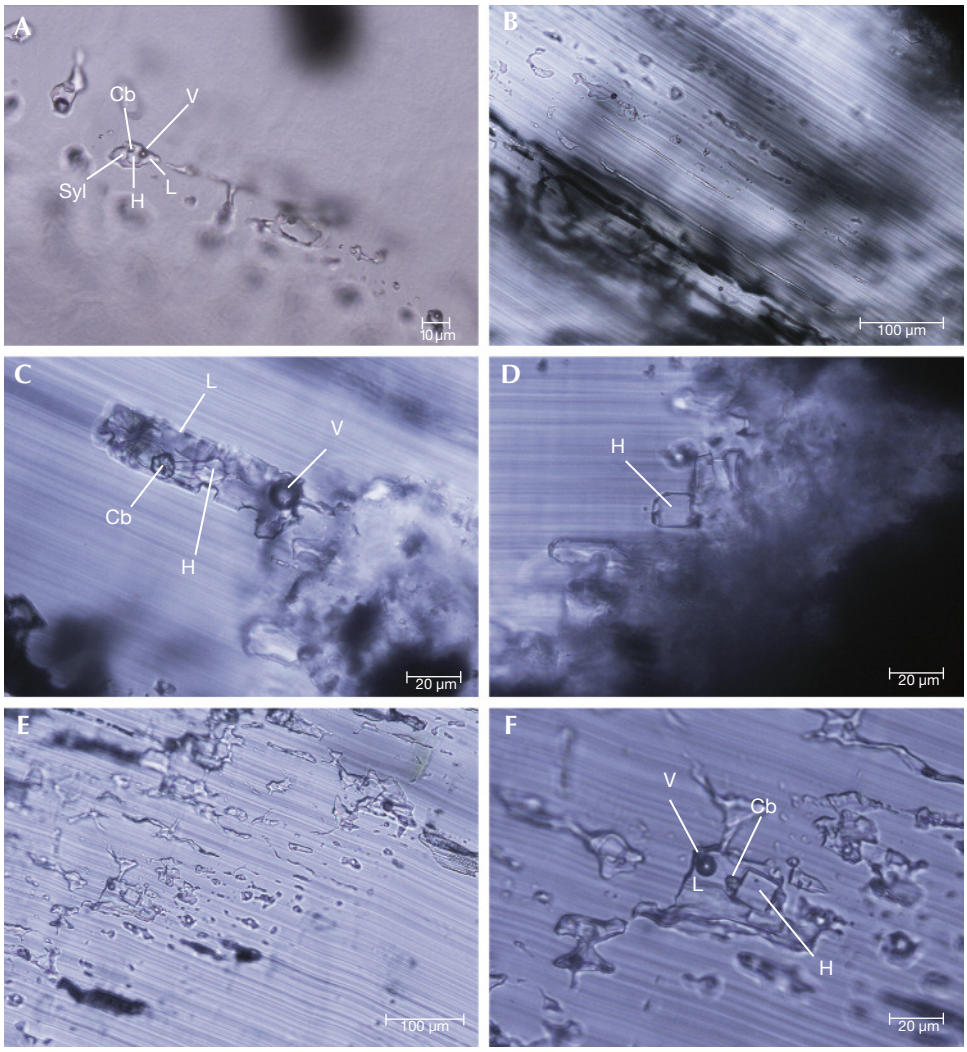

Figure 19. These multiphase fluid inclusions trapped in the arms of trapiche emeralds contain liquid (L) and vapor (V) phases as well as solid-phase daughter minerals (H = halite, Cb = carbonates, Syl = sylvite). A: This primary multiphase inclusion exhibits stretching and necking-down *phenomena. B: Alignment of multiphase fluid inclusions along the dislocation plane of the arm. C: A multiphase fluid inclusion trapped at the end of a dendrite (on the right) and parallel to the dislocations. D: A large cube of halite in a fluid inclusion cavity formed at the edge of the dendrites. E: Trails of multiphase fluid inclusions affected by necking-down. Re-equilibration of the cavities occurred during cooling, and some of the primary fluid inclusions became monophase (L or V) or biphase (V + L or L + H) cavities. F: Typical primary multiphase fluid inclusion in trapiche emerald, similar to those trapped by non-trapiche emerald.*

growth resumed and the pseudo-hexagonal shape was restored.

Rare multiphase fluid inclusions are observed in the core. They are similar to those found in the arms, indicating that the fluid composition was the same. However, multiphase fluid inclusions in the core are pseudo-secondary because they are often associated with fracturing.

Arms. Six arms with nearly identical size surround the core. They appear elongated in the $\langle 1\bar{1}0 \rangle$ directions and are bounded by the $\{10\bar{1}0\}$ faces. Sometimes a few arms are larger than others (figures 12E and 12F), making the trapiche asymmetric.

The color of the arms, like that of the core, can vary from pale (figures 12E and 12F) to intense green (figures 12D, 12H, 12K, and 12L) as a function of chemical composition (see "Trace-Element Analysis").

In each arm, bundles of straight dislocations develop perpendicular to the $\{10\bar{1}0\}$ faces (figures 18A and 18B). This indicates that they formed during the growth, in the direction of minimum elastic energy (Authier and Zarka, 1994). The direction of propagation of the dislocations in two adjacent growth sectors can be observed in figure 18C. Only in the trapiche of figure 12E do the dislocations appear slightly curved on the border of the largest arm. This is probably due to a change in the direction of minimum energy during the "anomalous" growth of this arm.

Solid and multiphase fluid inclusions are found in the arms. They are parallel to the dislocations (figures 18D, 19B, and 19E) and all located in proximity to the dendrites. The solid inclusions are similar to those found in the dendrites (see "Dendrites" below). The fluid inclusion cavities follow the extension of the dendrites in the arms. They are multiphase fluid inclusions containing daughter minerals, mainly halite

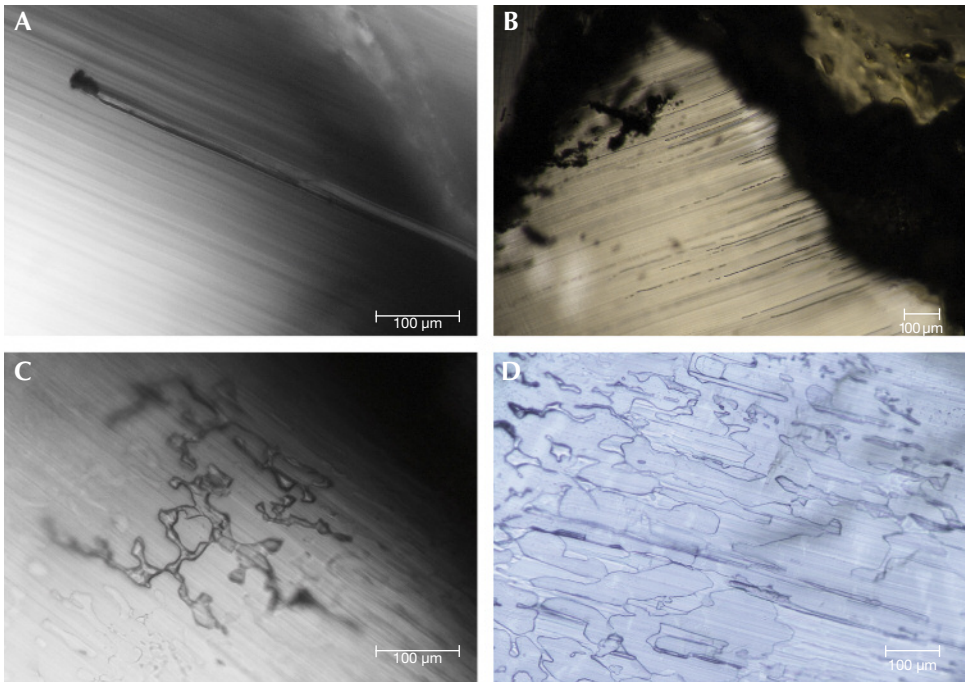

Figure 20. Elongated voids observed in the arms, perpendicular to the growth front and parallel to the dislocations. A: An elongated fluid inclusion cavity that formed parallel to the dislocation plane and after subsequent trapping of a solid inclusion (the black solid on the upper part of the cavity). B: Trails of voids parallel to the dislocation planes. C: Monophase fluid inclusions with highly irregular dendritic morphologies in the arms. D: Flat monophase fluid inclusions that developed along the dislocation planes.

but also carbonates and sylvite, liquid and vapor phases (figures 19A, 19C, and 19F). They belong to the H_2O-NaCl ± (CO_2) system already characterized for Colombian emerald-bearing veins (Roedder, 1963; Touray and Poirot, 1968; Kozlowski et al., 1988; Ottaway, 1991; Giuliani et al., 1991; Cheilletz et al., 1994). Sometimes, the multiphase fluid inclusions can be concentrated in certain portions of the arms, forming trails (figure 19E).

Evidence of heterogeneous trapping is observed in some multiphase fluid inclusions at the contact between dendrites and arms. This trapping is characterized by the presence of a large cubic crystal of halite (figure 19D) occupying more than 15 vol.% of the cavity and up to 70 vol.% (see "Emerald Mineralization" above).

Monophase fluid inclusions with highly irregular dendritic morphologies (figures 20C and 20D) are present in the arms. They do not contain solid or vapor phases. Similar inclusions were described in quartz crystals by Invernizzi et al. (1998) and interpreted as earlier-formed inclusions re-equilibrated at conditions of high *internal underpressure*. The dendritic morphology "results from the closure of the original inclusion void and preservation of fluid in long dendritic dissolution channels" (Invernizzi et al., 1998).

The arms contain elongated voids perpendicular to the growth front and thus parallel to the dislocations (figures 20A and 20B). Figure 20A shows that the formation of the elongated voids is related to the presence of solid inclusions. The voids resemble those described in Colombian emerald-bearing veins (Touray and Poirot, 1968) and in trapiche tourmaline (Schmetzer et al., 2011). Nevertheless, these voids may also have formed by dissolution along dislocation bundles if the *supersaturation* decreased after crystal growth (Scandale and Zarka, 1982; Authier and Zarka, 1994).

The arms are sometimes affected by fractures, filled by albite and small euhedral beryl crystals (figure 17B), that are synchronous with the arms' formation. The growth of the arms is not perturbed, because there is no discontinuity between the albite in the fractures and the albite in the dendrites on both sides of the arms.

In some emeralds, the arms have a fibrous texture like that of beryl in the dendrites (figure 21A), but in others they are not fibrous and appear similar to the core. Their different textures can reveal important information about the growth rates of the arms.

Dendrites. In trapiche emeralds, dendrites surround the core (figures 21B and 21F) and develop along the a-axis from the corners toward the outer edge with a herringbone texture (figure 21C). In particular, the dendrites may be larger near the edge, where they assume a characteristic fan shape (figures 21B and 21E). In some samples, the herringbone texture is not developed and the fan shape starts directly on the corners of the core. In this case, the dendrites are larger

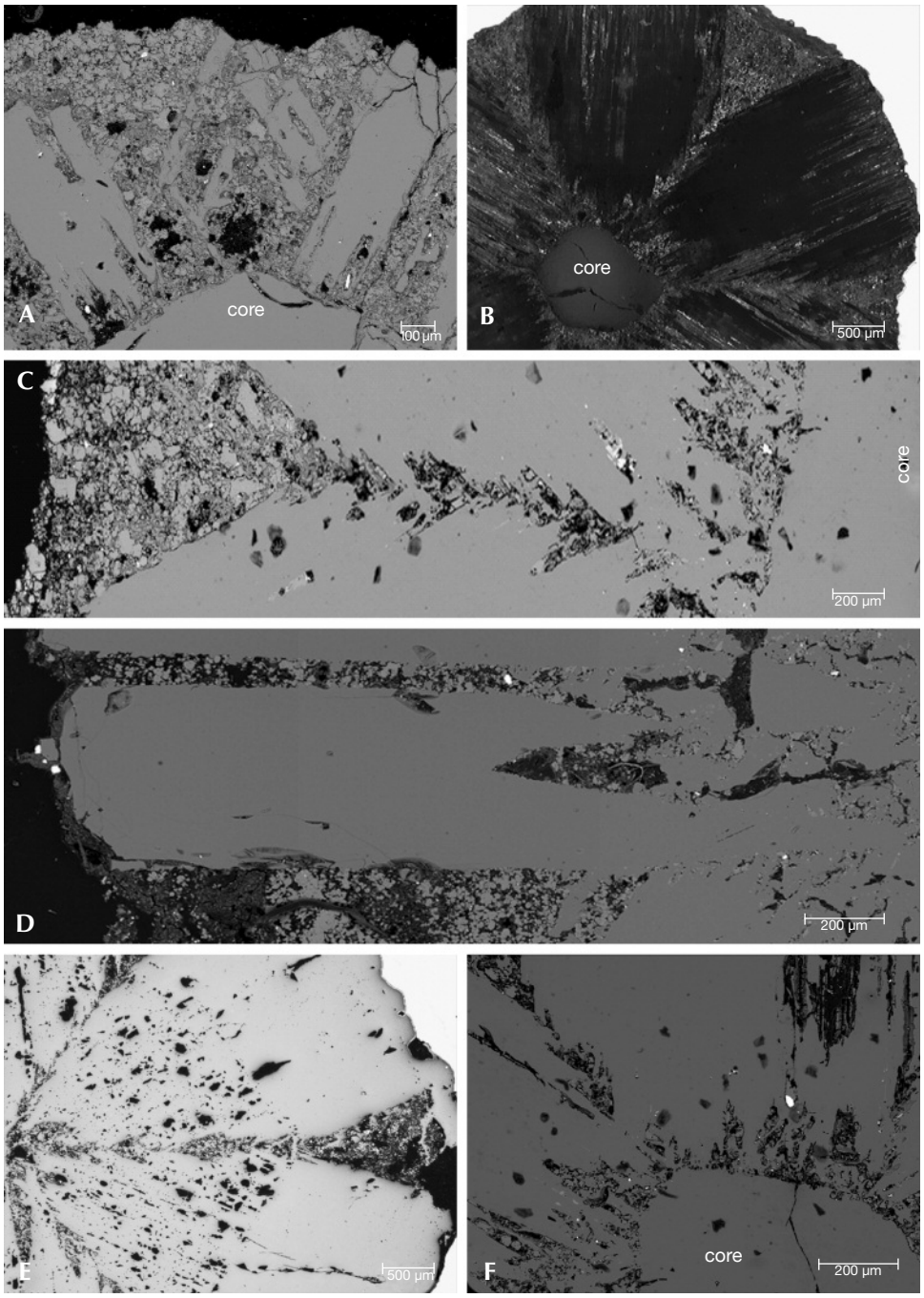

Figure 21. A: An SEM image of dendrites containing stringers of beryl intersecting at 60° angles. B: The dendrites are enlarged near the edge of the crystal, where they assume a characteristic chevron shape (see also images C–E). C: An SEM image of the typical herringbone texture of dendrites. The crystal formed on an albitized black shale matrix (on the left side of the image). D: This SEM image shows the presence of dendrites in the arms. E: Aspect of the dendrites from the core to the edge of the emerald crystal in a special section where the core is represented by a central point. The arms include albitized black shale (right side of the image), part of the matrix that supports the emerald. F: An SEM image of dendrites surrounding the core.

and contain stringers of emerald intersecting at 60° angles (figure 21A), as described by Chaudhari (1969). The dendrites may be present even in the arms (figures 12D and 12F) and parallel to the extension of the arms (figure 21D).

The dendrites are developed on albitized and calcitized black shales (figures 22A, 22B, 22D, and 22E), and sometimes rounded remnants of albitite are included in the calcite-bearing dendrites (figure 22C). In addition, variable quantities of organic matter are found in the albitites as well as in the dendrites (figure 22D), explaining why they often appear dark (figures 12B, 12C, and 12K). The X-ray computed 3D tomography image (figure 15D) of the trapiche emerald from figure 12H permitted the calculation of the dendrites' volume. The sample's total volume is 64.75 mm^3, of which 18% is occupied by the dendrites and 81% by the core and the arms, with the remaining 1% representing the porosity.

The dendrites contain mainly the albite and emerald assemblage, which explains why the den-

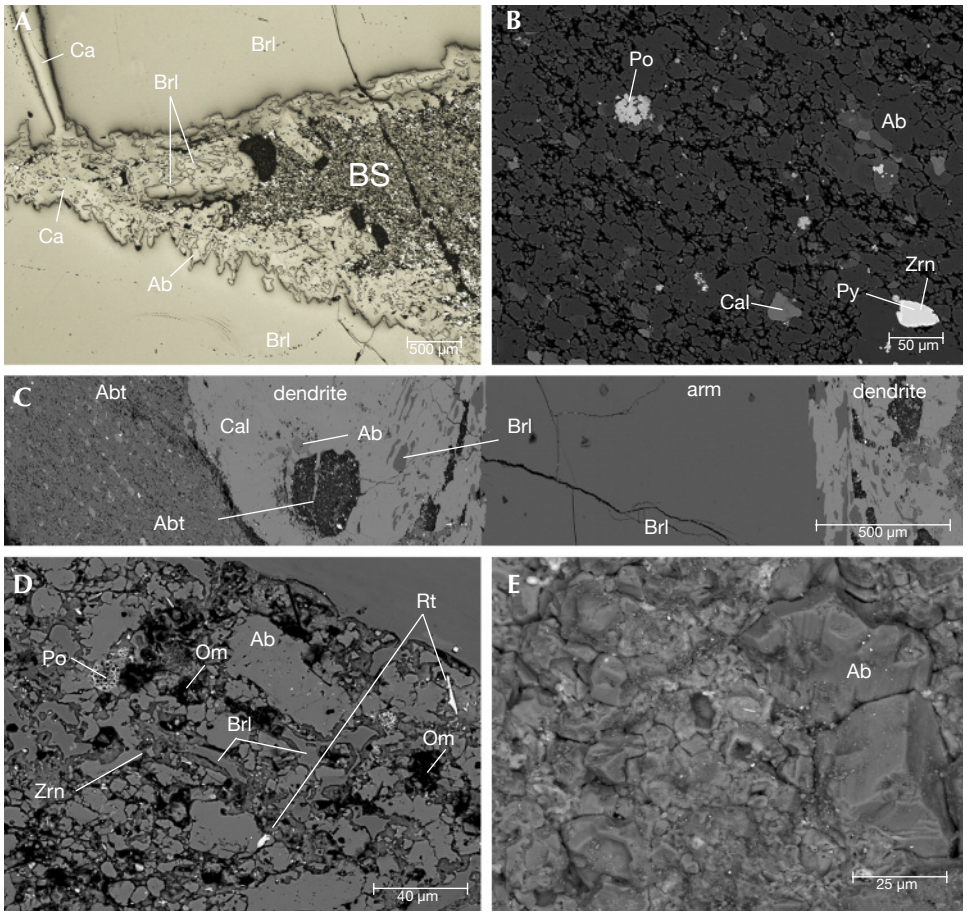

Figure 22. A: Microscopic image of dendrites formed on albitized (± calcitized) black shales (BS). The chevron-like habits characteristic of trapiche contain albite (Ab), emerald (Brl), and calcite (Cal). B: SEM image of the albitized black shale with albite, zircon (Zrn), calcite, pyrite (Py), and pyrrhotite (Po). C: SEM image of sample T4 showing the arm formed by emerald with dendrites on both sides. The dendrites are formed by calcite ± albite and emerald. The arm and the dendrites formed on albitite (Abt), a rounded remnant of which is included in the dendrite on the left side. D: SEM image of the albitite containing zircon, emerald, pyrrhotite with framboidal polycrystalline aggregates, rutile (Rt), and organic matter (Om). E: Morphology and size of albite crystals from the albitite, showing the rock's high porosity.

drite zones were also called "two-phase regions" by Nassau and Jackson (1970). The high quantity of albite (with or without calcite) makes the dendrites whitish, as shown in figures 12D and 12J. Quartz and dolomite complete the main paragenesis (figures 23A and 23B). Other solid inclusions characteristic of Colombian emeralds are found in minor amounts (figure 23C): rutile, carbonates (dolomite, ankerite, siderite), muscovite, fluorapatite, pyrite, pyrrhotite, zircon, fluorite, tourmaline, and minerals containing rare-earth elements such as monazite and parisite. Muscovite and rutile are V-bearing, and tourmaline usually shows complex zoning (figure 23D). The pyrrhotite forms *framboidal* polycrystalline aggregates typical of sedimentary sulfides.

Secondary alteration can affect the dendrites. The formation of clay minerals (mostly kaolin) and iron oxides/hydroxides modifies their original dark/whitish color to a brownish one (figures 12H and 12L). The typical evidence of alteration is the pseudomorphic replacement of framboidal sulfides by iron oxides/hydroxides. The alteration is favored by the elevated porosity of the dendrites, which is visible in the tomographic images of figure 15D.

Overgrowth. Overgrowth is not always present in trapiche emeralds. Its color is different from that of the adjacent arms, and it can be paler (figure 12F) or darker (figures 12A and 12G). The color difference indicates variations of V_2O_3 and Cr_2O_3 contents in the growth medium during the formation of the overgrowth (see "Trace-Element Analysis"). If many chemical changes occurred, the overgrowth becomes zoned, as in the trapiche shown in figure 12G. The contact between the overgrowth and the arms is often marked by the presence of inclusions.

X-ray Diffraction Topography. Even though X-ray diffraction topography is particularly suitable to investigate the strain associated with extended defects and to reconstruct the growth history of minerals (Agrosì et al., 2006; Agrosì et al., 2013), it has not been used until now to study trapiche emerald. This is probably because the technique requires the cutting of thin slices to minimize X-ray absorption, a drawback given the rarity of trapiche material. X-ray topographic images of trapiche emeralds are shown in figure 24. The samples' limited thickness kept us from preparing slices with different orientations, and only slices perpendicular to the c-axis were cut.

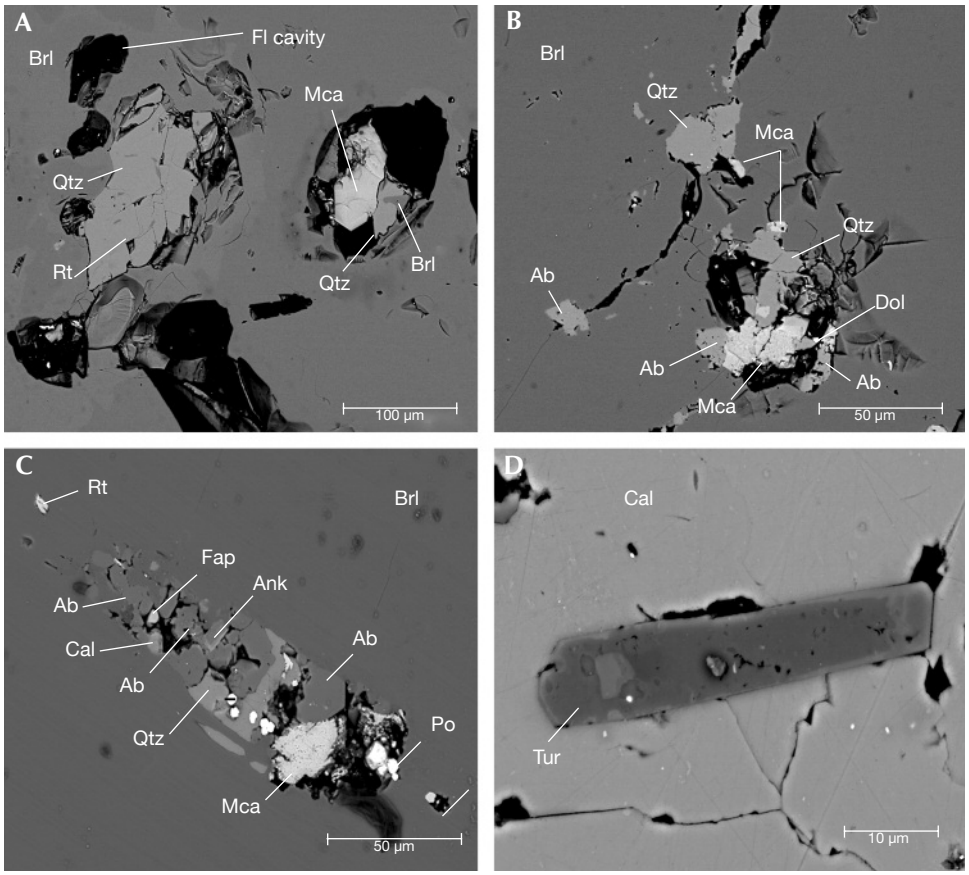

Figure 23. SEM images of inclusions found in dendrites at the contact with trapiche emerald arms. A: Aspect of the cavities filled by solids in the dendrites. The assemblages are formed by rutile (Rt) + quartz (Qtz), and quartz + emerald (Brl) + muscovite (Mca). B: Other mineral assemblages formed by dolomite (Dol) + albite (Al) + quartz + muscovite (Mca). C: Aspect of a dendrite cavity filled by albite, calcite (Cal), ankerite (Ank), muscovite, quartz, pyrrhotite (Po), fluorapatite (Fap), and rutile. The different solids are coeval, and the limits of some minerals show the presence of small fluid inclusion cavities, indicating that a fluid was bathing the whole cavity during dendrite formation. D: An SEM image of a tourmaline (Tur) crystal included in calcite.

Topographic images taken with *diffraction vectors* **g** of type *hki*0 show a strong diffraction contrast for the arms, while the core is almost invisible (figures 24A and 24C). In all arms, the presence of bundles of dislocations running perpendicular to the prismatic growth fronts is confirmed by the topographic images (figure 24). It was impossible to characterize these dislocations, because the orientation of the slices did not permit us to obtain topographic images with reflections suitable to determine the *Burgers vectors* applying the extinction criterion. The extinction criterion can be explained only referring to the diffraction contrast origin. The contrasts observed in the topographic images are due to the different intensities of diffraction between regions characterized by strain fields associated to the defects (kinematical effects) and almost perfect regions (dynamical effects). The diffraction contrasts can be extinct if the *scalar product* between the *diffraction vector* **g** and the vector representative of the strain field associated to the defect is equal to zero. In the case of dislocations, the extinction criterion is based on the scalar product $\mathbf{g} \times \mathbf{b} = 0$, where **b** represents the Burgers vector. It follows that the dislocations are out of contrast when **g** is perpendicular to **b**.

No diffraction contrast corresponding to the growth sector boundaries can be seen in the topographic images. Thus, the boundaries between the adjacent arms can be recognized only by means of the lack of contrast corresponding to the dendrites or by the directions of propagation of the dislocations in each arm (for example figures 24E, 24F, and 18C). This indicates that in trapiche emeralds there is a good interconnection between the different arms.

Topographic images taken with diffraction vectors inclined with respect to the c-axis (e.g., $\mathbf{g} = 12\bar{3}1$) show that the hexagonal core is also visible (figures 24B and 24D). The fact that both core and arms are visible in these topographic images indicates crystalline continuity between them, despite the presence of the dendrites.

The presence of dislocations in the core cannot be excluded, because the diffraction contrast observed (figure 24B) is not solely due to the fractures (slightly visible in figures 24A and 24C). It is worth noting that the contrast of these dislocations is always extinct on the topographic images with $\mathbf{g} = hki0$. On the basis of the extinction criterion, the **b** vector should thus be parallel to the c-axis, and one may suppose that the dislocations in the core are of screw type. This could be verified by a topographic study of the sections par-

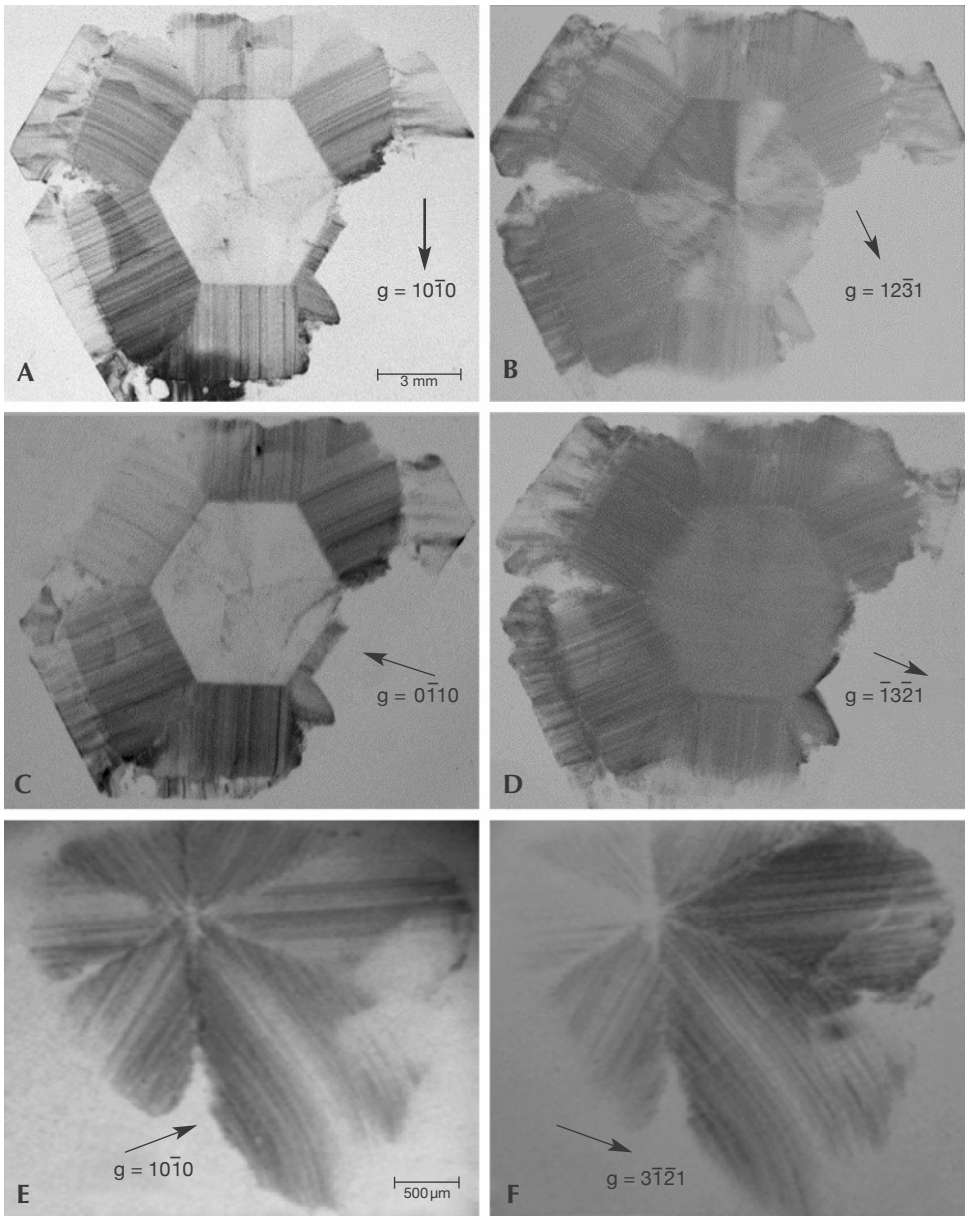

Figure 24. A to D: MoKα_1 X-ray topographic images of the trapiche emerald from figure 12G, taken with the diffraction vectors g = 10$\bar{1}$0 (A), g = 12$\bar{3}$1 (B), g = 0$\bar{1}$10 (C) and g = $\bar{1}$3$\bar{2}$1(D). E to F: X-ray topographic images of the trapiche emerald from figure 13E, taken with the diffraction vectors g =10$\bar{1}$0 (E) and g = 3$\bar{1}\bar{2}$1 (F).

allel to the c-axis, but unfortunately it was not possible to cut sections parallel and perpendicular to the c-axis from the same sample. For this reason, the presence of screw dislocations has not been confirmed.

Cathodoluminescence. CL images of the trapiche emerald samples exhibited several distinct features. The cold CL images obtained on the Peñas Blancas crystal (see figure 12D) show a crimson color due to the presence of Cr^{3+} and V^{3+} ions acting as the main CL activators (figure 25C). The cold CL image of the Muzo crystal (figure 25D) illustrates the color homogeneity of the core and the different textural and color aspect of the arms. These fibrous dendrites show variations in the reddish hue. Cold CL images obtained on the Coscuez crystal indicate that the core and arms have the same CL colors, but the dendrites formed by a fine intergrowth of albite, calcite, and emerald (figure 25D) have different CL colors for each: orange, yellow, and dark crimson for albite, calcite, and emerald, respectively. These CL colors could be explained by the presence of Mn in calcite (Ohnenstetter et al., 1998) and of Fe substituting Al in albite (Geake and Walker, 1975; White et al., 1986; Götze et al., 2000).

Trace-Element Analysis. Six sections of trapiche emerald from Coscuez, Peñas Blancas, and Muzo

TABLE 2. Representative chemical composition of trapiche emeralds from Coscuez, Muzo, and Peñas Blancas, obtained by electron microprobe analysis.

	Coscuez						Muzo				Peñas Blancas		
Oxides (wt.%)	T4-6 a	T4-1 d	T4-14 c	T11-1 a	T11-32 d	T11-23 c	T8-2 og	T8-11 og	T8-4 a	T8-13 c	T5-1 a	T5-10 d	T5-11 c
SiO_2	66.28	65.16	66.81	65.22	66.52	65.87	65.97	66.90	65.57	66.17	65.55	66.26	65.25
Al_2O_3	17.26	17.27	17.61	15.19	17.18	16.77	16.62	17.69	17.56	17.80	16.28	15.22	15.77
Cr_2O_3	0.17	0.18	0.12	0.80	0.95	0.62	0.29	0.72	0.05	0.02	0.90	0.68	0.30
Fe_2O_3	0.20	0.12	0.08	0.37	0.08	0.12	0.07	0.04	0.03	0.03	0.19	0.56	0.16
V_2O_3	0.27	0.27	0.14	1.08	0.82	0.67	0.64	0.30	0.05	0.03	0.87	1.17	0.68
BeO calc.[a]	13.79	13.56	13.90	13.57	13.84	13.71	13.73	13.92	13.64	13.77	13.64	13.79	13.58
MgO	0.58	0.53	0.55	1.28	0.33	0.65	0.99	0.29	0.73	0.69	0.71	1.40	1.47
Na_2O	0.56	0.50	0.45	0.98	0.27	0.49	0.97	0.25	0.45	0.43	0.61	0.59	0.76
H_2O calc.[b]	1.31	1.26	1.22	1.67	1.07	1.31	1.66	1.04	1.22	1.20	1.35	1.34	1.48
Total	100.42	98.85	100.88	100.16	101.06	100.21	100.94	101.15	99.30	100.14	100.10	101.01	99.45
Si	6.000	6.000	6.000	6.000	6.000	6.000	6.000	6.000	6.000	6.000	6.000	6.000	6.000
Al	1.841	1.874	1.864	1.647	1.826	1.800	1.782	1.870	1.894	1.902	1.756	1.624	1.709
Cr	0.012	0.013	0.009	0.058	0.068	0.045	0.021	0.051	0.004	0.001	0.065	0.049	0.022
Fe^{3+}	0.014	0.008	0.005	0.026	0.005	0.008	0.005	0.003	0.002	0.002	0.013	0.038	0.007
V^{3+}	0.020	0.020	0.010	0.080	0.059	0.049	0.047	0.022	0.004	0.002	0.064	0.085	0.050
Be^{2+} [b]	3.000	3.000	3.000	3.000	3.000	3.000	3.000	3.000	3.000	3.000	3.000	3.000	3.000
Mg	0.078	0.073	0.074	0.176	0.044	0.088	0.134	0.039	0.100	0.093	0.097	0.092	0.041
Na	0.098	0.089	0.078	0.175	0.047	0.087	0.171	0.043	0.080	0.076	0.108	0.104	0.135
Total	11.063	11.078	11.040	11.161	11.050	11.077	11.159	11.027	11.083	11.077	11.103	11.089	11.125
V/Cr	1.58	1.49	1.16	1.34	0.86	1.07	2.19	0.41	0.99	1.49	0.96	1.71	2.25

[a] *Amount of Be inferred from stoichiometry zones of the trapiche emerald: a = arm; d = dendrite; c = core; og = overgrowth.*
[b] *Calculated following the equation $H_2O = (0.84958)(Na_2O) + 0.8373$ (Giuliani et al., 1997).*

were analyzed by EPMA and with elemental compositional EDX maps in order to evaluate chemical composition, zoning, and color variations in the core, dendrites, arms, and overgrowths (tables 1–3). Overall, the emeralds contained relatively low concentrations of Fe_2O_3, from 200 to 5700 ppm. The Na_2O

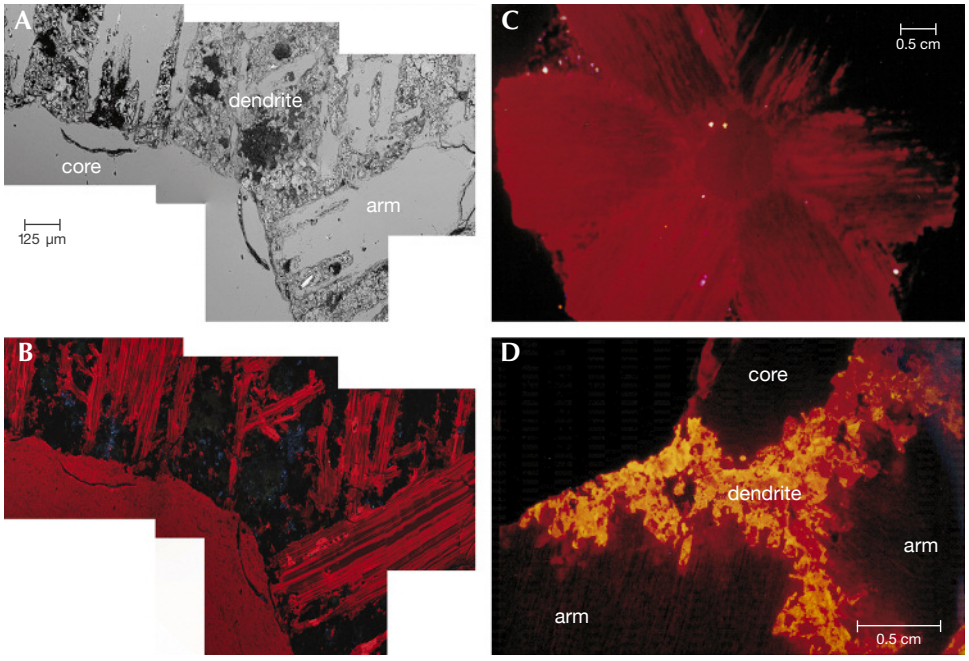

Figure 25. A and B: SEM and CL images of a Muzo sample show that under CL, the core is homogenous and appears crimson-colored due to the presence of Cr^{3+} and V^{3+} ions acting as the main CL activators. The arms, on the other hand, are fibrous and show variations in the reddish hue. C: The cold CL image of a Peñas Blancas sample shows the homogeneity of its red color due to the presence of the V and Cr chromophores. D: The cold CL image of a Coscuez sample reveals different CL colors: orange for albite, yellow for calcite, and dark crimson for emerald.

TABLE 3. Representative chemical composition of trapiche emeralds from Coscuez and Muzo[a], obtained by electron microprobe analysis.

	Coscuez						Muzo						
Oxides (wt.%)	T11-25 c	T11-20 c	T11-33 d	T11-28 d	T11-1 a	T11-4 a	T10-1 center	T10-8 c S	T10-12 c N	T10-7 a S	T10-5 a S	T10-3 a S	T10-16 a N
SiO_2	66.36	65.37	66.07	65.59	65.22	65.34	66.50	65.50	66.21	66.38	66.57	65.71	66.29
Al_2O_3	16.49	16.15	15.87	16.32	15.19	16.15	18.20	16.20	17.26	17.68	17.37	17.41	17.93
Cr_2O_3	0.60	0.49	0.87	0.63	0.80	0.73	0.09	0.12	0.05	0.05	0.11	0.03	0.03
Fe_2O_3	0.10	0.11	0.19	0.09	0.37	0.21	0.08	0.51	0.10	0.13	0.23	0.26	0.20
V_2O_3	0.72	0.59	0.89	0.58	1.08	0.87	0.15	0.26	0.13	0.20	0.21	0.21	0.20
BeO calc.[b]	13.81	13.60	13.75	13.65	13.57	13.60	13.84	13.92	13.78	13.81	13.85	13.67	13.79
MgO	0.75	0.98	1.21	0.67	1.28	0.86	0.67	1.48	0.90	0.57	0.87	0.82	0.67
Na_2O	0.66	0.78	0.86	0.55	0.98	0.64	0.56	1.13	0.63	0.39	0.69	0.67	0.56
H_2O calc.[c]	1.39	1.49	1.56	1.30	1.67	1.38	1.31	1.79	1.87	1.10	1.42	1.40	1.31
Total	100.88	99.56	101.27	99.38	100.16	99.78	101.40	100.91	100.93	100.31	101.32	100.18	100.98
Si	6.000	6.000	6.000	6.000	6.000	6.000	6.000	6.000	6.000	6.000	6.000	6.000	6.000
Al	1.757	1.747	1.699	1.760	1.647	1.748	1.935	1.749	1.843	1.883	1.845	1.874	1.913
Cr	0.043	0.036	0.062	0.046	0.058	0.053	0.006	0.009	0.004	0.004	0.008	0.002	0.014
Fe^{3+}	0.007	0.008	0.013	0.006	0.026	0.015	0.005	0.035	0.007	0.009	0.016	0.018	0.014
V^{3+}	0.052	0.043	0.065	0.043	0.080	0.064	0.011	0.019	0.009	0.014	0.015	0.015	0.015
Be^{2+} [b]	3.000	3.000	3.000	3.000	3.000	3.000	3.000	3.000	3.000	3.000	3.000	3.000	3.000
Mg	0.101	0.134	0.164	0.091	0.176	0.118	0.090	0.202	0.122	0.077	0.117	0.112	0.090
Na	0.116	0.139	0.151	0.098	0.175	0.114	0.098	0.201	0.111	0.068	0.121	0.119	0.098
Total	11.076	11.107	11.154	11.043	11.161	11.111	11.146	11.215	11.096	11.056	11.121	11.139	11.144
V/Cr	1.19	1.20	1.02	0.91	1.34	1.18	1.66	2.15	2.58	3.97	1.90	6.95	6.62

[a] *Analyses on Coscuez samples were performed on a section perpendicular to the c-axis. Analyses on Muzo samples were conducted on a section parallel to the c-axis.*
[b] *Amount of Be inferred from stoichiometry zones: a = arm; c = core; d = dendrite; S = southern part of the crystal; N = northern part of the crystal.*
[c] *Calculated following the equation $H_2O = (0.84958)(Na_2O) + 0.8373$ (Giuliani et al., 1997).*

concentrations were between 1400 and 15,500 ppm, which corresponds to a calculated H_2O in the channels between 0.95 and 2.15 wt.%, following the equation proposed by Giuliani et al. (1997). In terms of chromophores, V was the main element; the highest concentrations in V_2O_3 and Cr_2O_3 were 11,700 and 9,700 ppm, respectively. The V/Cr ratio was between 0.42 and 6.9 (tables 2 and 3). Some of the emeralds were Cr-free, with V_2O_3 content up to 1.17 wt.% (sample in figure 12D; table 2). The Mg contents were between 2,300 and 14,800 ppm.

Chemical compositional EDX maps of trapiche from Muzo (sample T8 in figure 12G) were obtained on a section perpendicular to the c-axis (figure 26A). This sample contained a colorless to very light green core rimmed by dendrites and six colorless arms (figure 12G). The arms were rimmed by deep green overgrowth zones. All the chemical elements of emerald were distributed homogenously in the EDX-map of the core and arms. The dendrites were characterized by Na anomalies that correspond to minute crystals of albite formed during their growth. The overgrowth zones were richer in Mg and Na, with important Cr and V anomalies, than the core and arms. The contact zone between the arm and the overgrowth was sharp and distinguished by a Cr-rich zone (figure 26F). The Al anomalies detected at the border and within the fractures of the crystal were due to argillites that formed during a late *meteoric water* stage.

The distribution of the different chemical elements in the various maps were coupled to the chemical distribution of Cr and V (in wt.%). EPMA analyses presented in table 2 show that the arms were richer in Cr and V than the core. The contact zone between the arms and the overgrowth was sharp and indicated by a Cr-rich zone in the EDX image (figure 26F). The Cr_2O_3 and V_2O_3 contents calculated by EDX reached 0.72 and 0.64 wt.%, respectively.

Sample T10 is a section parallel to the c-axis of a V-rich greenish trapiche emerald from Muzo (figure 27A). The chemical composition of the center, the core, and the rims are reported in table 3. The spatial distribution of V and Cr in the longitudinal section showed a positive correlation between these two elements for the center and the core (figure 27B). The arms from both sides of the crystal had a restricted V_2O_3 range (table 3).

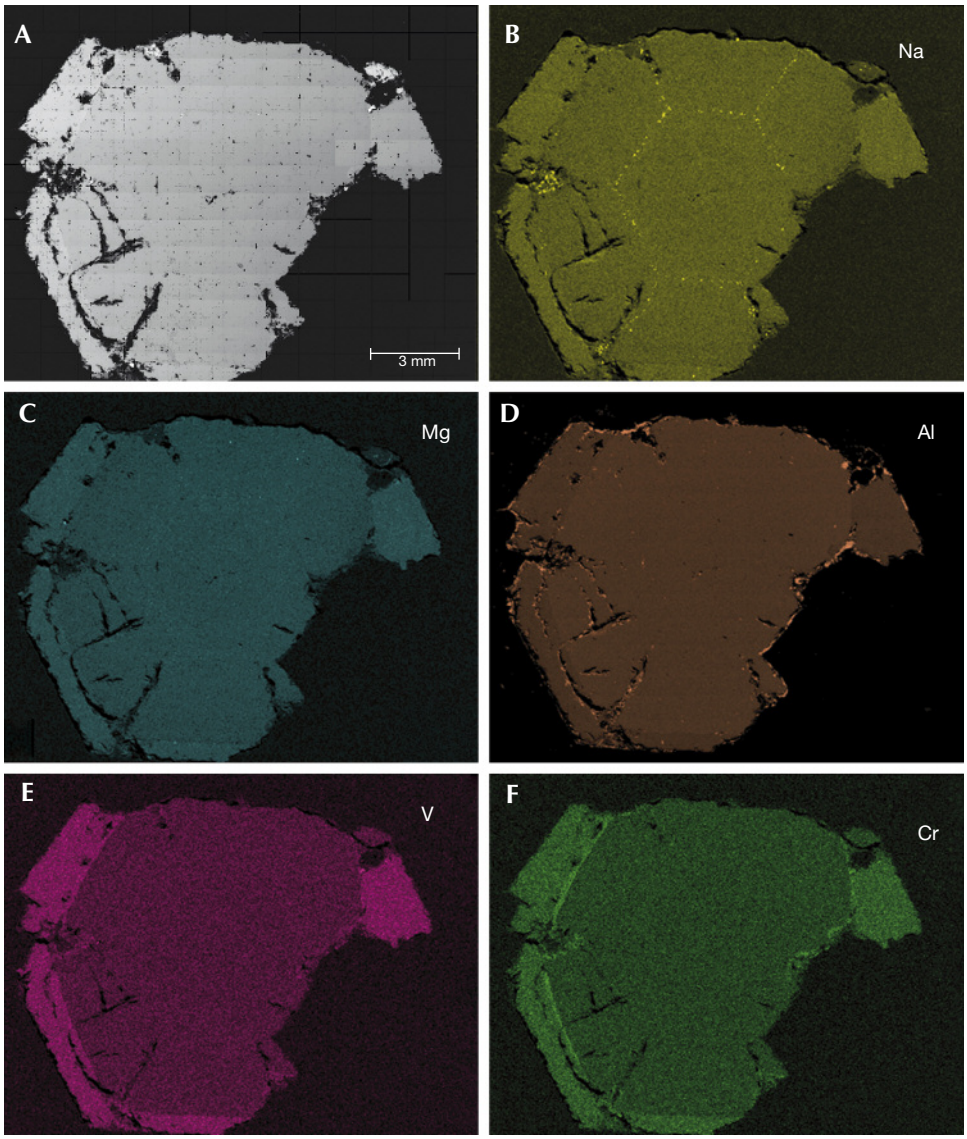

Figure 26. A: An SEM view of sample T8 from Muzo (shown in figure 12G). B–F: EDX elemental maps show the distribution of sodium (B), magnesium (C), aluminum (D), vanadium (E), and chromium (F). Brighter color corresponds to a higher concentration of the element being imaged. Image B shows a very high concentration of Na in the dendrites where albite is present. Image C shows a slight increase of Mg in the overgrowth zone. Image D shows important concentrations of Al in the fractures filled by clay minerals during late meteoric fluid circulation. Images E and F show that there is no chemical difference in the distribution of V and Cr between the core and the arms: Both areas are very poor in chromophores (Cr and V <600 ppm), although the overgrowth zone is very rich in V and Cr: This area has the "green grass" color of Muzo emeralds. The emerald zone in contact with the arms is Cr-rich (up to 7200 ppm), while the outer zone is V-rich (up to 6400 ppm).

DISCUSSION

The formation of trapiche emerald was approached by a combination of previous and new experimental data on the trapiche texture with the constraints of tectonics and basinal fluid circulation in a sequence of black shales of the western emerald zone in Colombia's Eastern Cordillera.

Growth History. While many hypotheses have been proposed, how and why trapiche emeralds formed will be elucidated on the basis of new experimental data presented in this work. These data further confirm that trapiche emeralds are neither composite (Chaudhari, 1969) nor twinned crystals (Codazzi, 1915; Bernauer, 1933). The possibility that trapiche emeralds are made of three intersecting crystals elongated in the <1$\bar{1}$0> directions and that the spaces between them are filled by dendrite material is excluded by the presence of the dendrites around the core (see, for example, figures 14 and 15). Moreover, X-ray topographic images show crystalline continuity between the arms and the core, indicating they are not several crystals but portions of the same emerald. The trapiche emerald is thus a unique crystal formation, as already stated by Nassau and Jackson (1970). Furthermore, the presence of multiphase fluid inclusions in the trapiche emeralds similar to those observed in non-trapiche Colombian emeralds suggests that they formed from the same fluid in the system, H_2O-NaCl ± (CO_2).

The chemical composition of the interstitial fluid, the temperature (approximately 300–330°C), and the bulk composition of the rocks (i.e., albitized black shales) are the same for trapiche emerald and emerald-

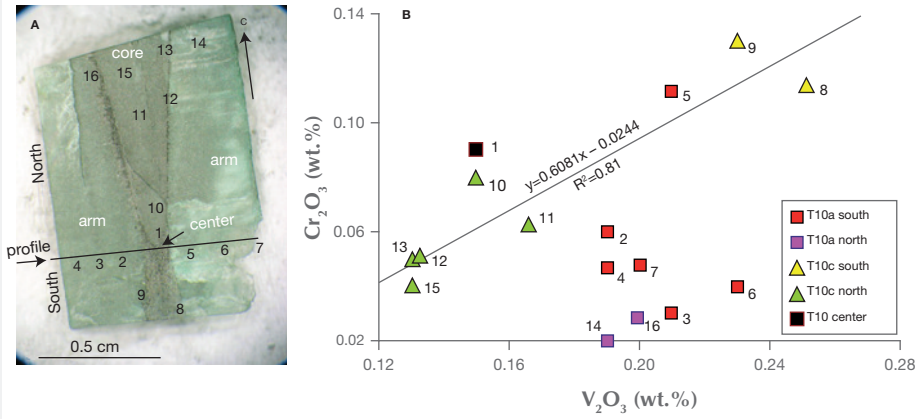

Figure 27. Variation of vanadium (V_2O_3) and chromium (Cr_2O_3) contents (in wt.%) in the trapiche emerald from Muzo presenting a section parallel to the c-axis (see table 3). A: The different points of analyses are reported from 1 to 16 in the core (pts. 1, 8–10, 11–13, and 15) and the two arms (pts. 2–7, 14, and 16). B: Variation of the V_2O_3 and Cr_2O_3 contents in the core and the arms of the sample.

bearing veins. The difference in the texture between these two is due to extreme variation of pressure in the history of their formation. That trapiche formed before regular emerald is evidenced by field observation. Trapiche emerald developed on albitized black shale that is crosscut by regular-emerald-bearing veins and tension gashes. Some of the trapiche have an overgrowth zone that undoubtedly grew during the formation of non-trapiche emerald. The tectonic decompression increased the degree of supersaturation, allowing the formation of trapiche emeralds, whereas emerald overgrowths occurred at a lower degree of supersaturation, until finally, at equilibrium conditions, euhedral non-trapiche emerald grew in the veins.

The trapiche emeralds started growing at the beginning of the local decompression. The hydrothermal fluid came in contact with the albitized black shale matrix, favoring the formation of seed crystals of emerald. During the growth of these seeds, textural sector zoning—i.e., the accumulation of inclusions derived from the matrix along the interfaces of growth sectors (Andersen, 1984)—took place. This is proved by the presence of dendrites all around the core (pinacoidal growth sectors) and between the arms (prismatic growth sectors).

Textural zoning can also occur with chemical sector zoning, in which the growth sectors have different chemical compositions. In both cases, the growth sectors can be easily recognized. They are separated by inclusions in textural sector zoning, and by composition and color differences in chemical zoning. This is the case with some trapiche samples analyzed in this study showing different concentrations of V and Cr in the core and the arms (tables 2 and 3). Different amounts of chromophore elements can result in different colors of various sectors, as in sample T4 (figure 12C), where the core is very pale green and the arms are green (richer in both Cr and V). The higher quantity of V and Cr also suggests that the arms grow faster than the core. The faster growth causes the de-

Figure 28. Schematic representation of trapiche texture in Colombian emeralds, formed by textural sector zoning and displacement growth.

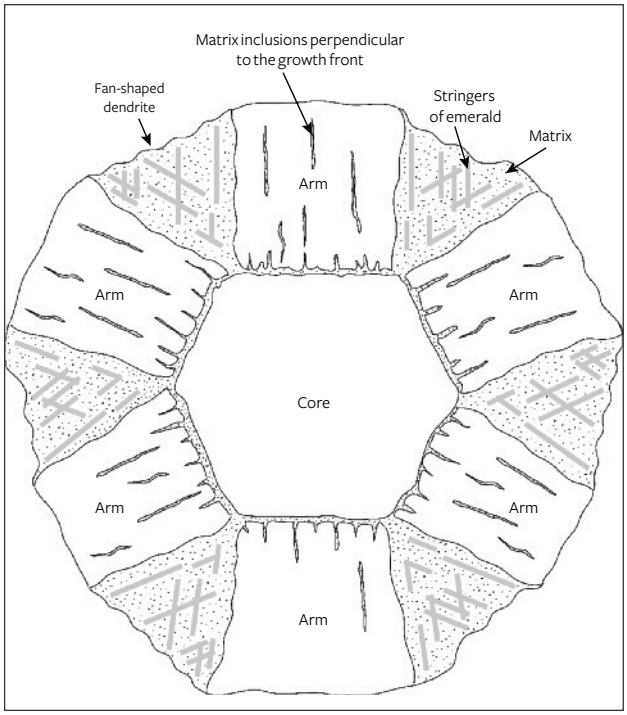

pletion of Al in the fluid near the prismatic growth fronts, allowing the incorporation of metal elements in the octahedral site to allow the growth's front to advance. The faster growth of arms is supported by the higher quantity of defects perpendicular to the growth fronts such as bundles of dislocations and solid and multiphase fluid inclusions (figures 20 and 24).

The overpressure and associated fluid supersaturation allow emerald to continue its growth and favor the displacement growth pushing the matrix material from the growing faces (Yardley, 1974; Carstens, 1986; Riche and Mitchell, 1991). Two factors are necessary for displacement growth: high fluid pressures and slow growth (Yardley, 1974). Because the core grows slower than the arms, it pushes away the matrix material that accumulates around it as dendrites (figure 28).

The matrix material is also displaced by the prismatic growth sectors. Nevertheless, the matrix cannot be moved away as fast as these sectors grow. Thus the matrix is trapped, forming dendrites within and/or along the arms and perpendicular to the growth fronts (i.e., parallel to the elongation direction of the arms; see figures 12D and 21D). It should be noted that the matrix material is trapped primarily along the a-axis, forming dendrites whose size is a function of the quantity of displaced material (figure 12). The crystallographic orientation of the dendrites can be explained by the Berg effect (1938). Because the driving force is higher on the corners than on the faces, the emerald can grow so fast as to trap most of the matrix material along the a-axis. The fan-shaped dendrites observed in some trapiche emeralds are common in trapiche chiastolites and garnets (Riche and Mitchell, 1991; Rice, 1993) and are also known as "re-entrants" (Pogue, 1916). Fan-shaped dendrites are also considered nucleation zones for minor growth (Rice, 1993), explaining why in some dendrites the stringers of emerald develop parallel to the edges of prismatic sectors and intersect at 60° angles (figure 21A). This 60° angle is not arbitrary and indicates that the emerald grows parallel to the two prismatic sectors delimiting the fan-shaped dendrite. The rapid growth along the a-axis is also proved by the fact that the stringers of emerald have a tree-like, fibrous texture (figures 25A and 25C).

During displacement growth, the black shales played a key role in the thermal reduction of sulfate by oxidizing the organic matter. Oxidation generated CO_2, creating fluid overpressure in the black shale. Such exothermic reactions produced hydrothermal carbon (bitumen), which can float in the fluid as a syngenetic material and concentrate in the dendrites.

Overpressure can explain the presence of fractures in the core and arms (see "Results" for details) filled with the same materials observed in the matrix. It can also account for the plastic deformation of the core that results in an *undulatory extinction* under cross-polarized light in some samples.

Overpressure can also cause a change in the chemical composition of the growth medium, leading to the dissolution of the emerald not yet in equilibrium with these new conditions. Consequently, partial dissolution affects some portions of growing crystals. This kind of "selective" dissolution (etching) has been described by Bernauer (1933) on some trapiche emeralds from Muzo. It has been observed by Lyckberg (2005a,b) on the prismatic faces of heliodor from Karelian, Russian, and Ukrainian pegmatites, and by Tempesta et al. (2011) on beryl crystals from Minas Gerais, Brazil.

After decompression and hydraulic fracturing, the degree of supersaturation of the fluid decreased considerably. This can favor the formation of an overgrowth surrounding the core, the arms, and the dendrites. The lower degree of supersaturation can also explain the formation of elongated voids in the arms by dissolution along the dislocation bundles (Scandale and Zarka, 1982; Authier and Zarka, 1994).

Geological History. The emerald-bearing veins in Colombia's western emerald zone formed in a context of fluid pressure variations in tear faults and thrusts affecting the Lower Cretaceous black shales. Formed along tear faults were numerous veins and hydraulic breccias. They resulted from the fracturing of the wall rocks during a tear fault increment (a displacement along the fault plane, likely inducing a seismic event). This increment is responsible for development of dilational *jogs* along several fault segments. As a result, the jogs caused a large fluid pressure gradient and "pumped" the surrounding hydrothermal fluids. Blocks of black shales, white albitite, and albitized and/or carbonatized black shales simultaneously collapsed into the jog and were cemented by carbonates and albite.

Along the thrust, the fault propagation is achieved by shear-tensional failure caused by hydraulic fracturing under supra-lithostatic fluid pressure and small differential effective stresses (box C). The polygenetic nature of the fragments of the breccia such as in the tear faults, and the rotations and partial dissolution of the elements, clearly indicate bulk transport of mate-

BOX C: GEOLOGICAL MODEL FOR THE PROPOSED MECHANISM OF TRAPICHE EMERALD FORMATION

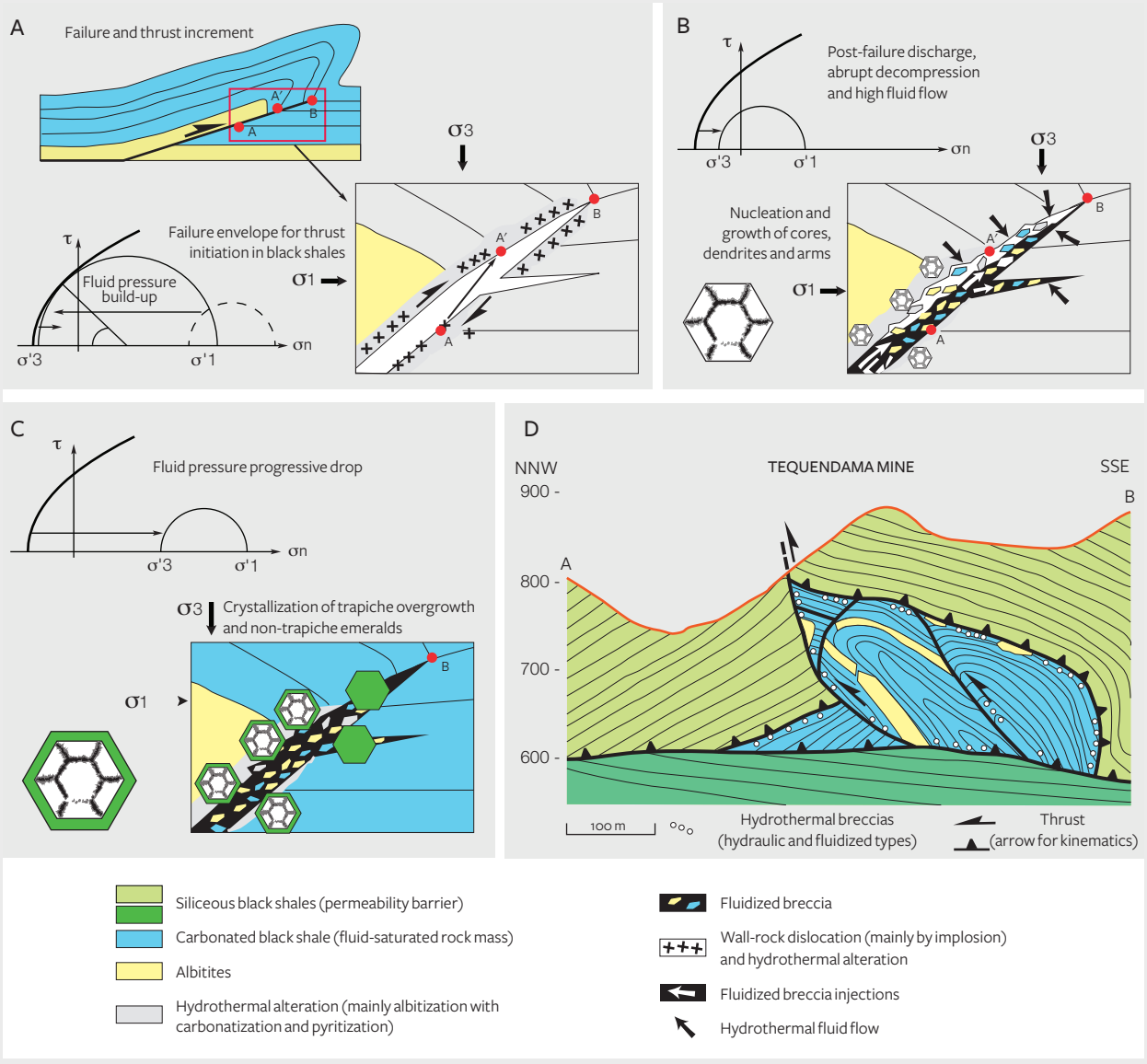

Figure C-1. Geological model for the proposed mechanism of the trapiche emerald formation from the western emerald zone. A: Thrust propagation and failure. B: Nucleation and growth of core, dendrites, and arms of trapiche emerald. C: Formation of trapiche overgrowths and regular emerald in veins. D: Cross-section of the Tequendama mine. In the Mohr's circle diagrams in A, B, and C, τ = shear stress; σn = normal stress; σ1 and σ3 = the main stresses.

rial during fluid flow (*fluidization phenomena*). The cement is formed by carbonates, pyrite, and albite, creating the hydrothermal breccia called "cenicero." The fluidized breccias are associated with emerald-bearing thrust veins, which are horizontal tension gashes in this compressive tectonic context. The sealing of faults by carbonate deposition and cementation of the fluidized breccia depends on the elapsed time between

The formation of Colombian trapiche emerald is closely related to the structural geology history in the western zone. The correlation between the formation of tear faults under compressional stress and the growth of trapiche emerald can be elucidated in the following three steps (figure C-1: A, B and C):

- A: Thrust propagation and failure. The *incremental thrust propagation* is related to the highest fluid pressures, which caused the failure and propagation of the fault (from point A to point A'). The failure occurred in the hybrid-shear-extensional mode, the thrust presenting a dilatant component. Physically, the *Mohr's circle* moved to the left and touched the failure envelope of the black shale material.
- B: Abrupt decompression of fluid pressure is related to the opening of dilatant sites (i.e., high permeability and porosity zones) along the thrust. Hypersaline Na-bearing fluids responsible for strong albitization of the hosting carbon-rich black shales are "pumped" into those dilatant zones with high flow rates. As a result, high fluid pressure gradients also triggered fluidization processes responsible for the formation of polygenic breccia. Physically, the Mohr's circle describes an incipient rightwards motion. This decompression caused an increase of the driving force of the emerald crystal growth. The emerald seed crystals grew on albitized black shales. During the growth of these seeds, textural sector zoning of trapiche emerald took place with the dendrites all around the core and between the arms.
- C: Formation of trapiche overgrowths and non-trapiche emeralds during a progressive decrease of pressure and flow (i.e., lower fluid pressure gradient than in B). Non-trapiche emeralds are mainly hosted within sub-horizontal extensional veins and fluidized hydrothermal breccias.

In diagram D in figure C-1, a cross-section of the Tequendama mine following the geological map in figure 6 illustrates the relationship between structures and trapiche growth. The cross-section shows the different lithologies and tectonic structures described in the text. The thrusts and tear faults (represented in figure 6) are associated with the breccias, sub-horizontal extensional veins, and potential zones related to trapiche emerald.

the drop and the following build-up of fluid pressure. The thrusts propagate in a succession of faulting, fluid flow (multistage events), hydrothermal alteration, and emerald deposition (Branquet et al., 1999b).

Trapiche emerald (figure 29) formed when the fluid pressure exceeded the *lithostatic pressure* (box C). The local decompression induced the supersaturation of the hydrothermal fluid and an increase of the driving force of the emerald crystal growth (stage 1 under "Emerald Mineralization"). The emerald seed crystals grew on albitized carbon-rich black shale (see box C, figure C-1) or albitite (the type seen at Peñas Blancas; Vuillet et al., 2002), as argued by the presence of solid inclusions and matrix around the trapiche cores (Bernauer, 1933; Nassau and Jackson, 1970). Stage 1 is also associated with the formation of tension gashes and thrust-fluidized breccias ("cenicero") and thrust veins.

The hydrothermal fluid bathed each whole cavity, and the precipitation of carbonates, pyrite, and albite sealed the fault open spaces (hydrothermal breccia), and emerald deposition occurred with its carbonate-pyrite assemblage in the thrust veins (stage 2). During this last episode of emerald crystallization in the veins, the degree of supersaturation of the fluid decreased considerably up until chemical equilibrium. During this time, the trapiche emeralds probably acquired their final deep-green overgrowths, also found in non-trapiche emerald-bearing thrust veins.

CONCLUSIONS

Trapiche emeralds occur in association with black shales in the western emerald zone of Colombia's Eastern Cordillera Basin. They formed in a geological context of fluid pressure variations along faults and thrusts affecting the Lower Cretaceous sedimentary series. The fluid accumulation at the faults' tip led to maximum fluid overpressure and subsequent decompression. The rocks failed, and trapiche emerald formed in the albitized black shale host rock, followed by the crystallization of emerald in carbonate veins.

Trapiche emeralds from Muzo, Coscuez, and Peñas Blancas were investigated by several analytical techniques in order to propose a model of formation for trapiche texture linked to the structural geology of the deposits. Petrographic and SEM observations combined with X-ray topography and tomography images confirmed that trapiche emerald is a single crystal formed by different zones: a core (pinacoidal growth sectors), dendrites, and arms (prismatic growth sectors), sometimes surrounded by an overgrowth. The color of these zones is due to the presence of V and lower concentrations of Cr, although both elements were detected by EPMA even in colorless zones such as some of the cores.

Figure 29. These trapiche emeralds, all from Peñas Blancas, range from 5.09 to 22.74 ct. Photo by Robert Weldon/GIA. Courtesy of Jose Guillermo Ortiz, Colombian Emerald Co.

The formation of the trapiche texture in Colombian emeralds is controlled both by the peculiar "structurally controlled" genesis of the deposits and by the crystal symmetry, determining which growth sectors develop and how many of them. From this, a few crucial points on trapiche formation can be summarized:

1. The growth of trapiche emerald started during the local decompression responsible for the supersaturation of the fluid. The hydrothermal fluid came in contact with the black shale matrix, favoring the formation of emerald crystal seeds.
2. Textural sector zoning, sometimes associated with chemical sector zoning, took place during the growth of these seeds. The inclusions of black shale matrix were incorporated between the growth sectors, forming the dendrites around the core and between the arms.
3. The emeralds continued their growth, displacing the matrix material from the growing faces. As a result, the matrix may also be trapped in the arms perpendicular to their growth fronts, even if it is preferentially incorporated along the a-axis. The dendrites between the arms have a typical fan-shape near the borders of the samples, because the emerald grows faster along the a-axis than along $\langle 1\bar{1}0 \rangle$ (see again figure 13), and thus a higher quantity of matrix material can be trapped.
4. An overgrowth, generally of gem quality, may be formed after decompression. This overgrowth surrounding the core, arms, and dendrites and restoring the emeralds' euhedral habit. During overgrowth formation, non-trapiche emerald formed in the carbonate veins.

For the first time, the development of the trapiche texture has been related to the geological conditions of Colombian emerald deposits. Although some formation models were previously proposed for trapiche minerals, they were extrapolated from the deposit context and were not supported by geological events responsible for the supersaturation of the mineralizing fluids.

ABOUT THE AUTHORS

Dr. Pignatelli, a geologist and expert in mineralogy and crystallography, is currently a postdoctoral researcher at the University of California, Los Angeles. Dr. Giuliani is director of research at the Institute of Research for Development (IRD) in Toulouse (GET) and the French National Center of Research (CRPG/CNRS) in Vandœuvre. He is recognized for his work on the geology, geochemistry, and genesis of several colored stone deposits. Dr. Ohnenstetter is a retired geologist based in Marinville-sur-Madon, France, formerly with CRPG/CNRS, who specializes in petrology and cathodoluminescence spectroscopy and mineralogy. Dr. Agrosì is a researcher with the Department of Earth and Geo-environmental Sciences at the University of Bari, Italy. Ms. Mathieu specializes in quantitative analyses using EDX and WDX spectrometry in complex systems at GéoRessources 7359 research unit, Vandœuvre, France. Mr. Morlot is responsible for X-ray tomography applied to Geosciences at GéoRessources 7359 unit, Vandœuvre, France. Dr. Branquet is an assistant professor of earth sciences at the University of Orléans in France.

ACKNOWLEDGMENTS

The authors would like to thank Omar Bustos Santana, who collected and provided the trapiche emerald samples used in this study. We thank also the manuscript reviewers for their helpful and constructive suggestions.

GLOSSARY

Albitite: a magmatic or metasomatic (see *metasomatism*) rock composed almost wholly of coarse- to fine-grained crystals of albite.

Basinal brine: fluids in basins that are enriched Na, Ca, and Mg sulfates. In basins, processes of sediment or basin dewatering give rise to large volumes of fluids moving through different types of rocks (generally sedimentary). The temperature increases to 80°–200°C or higher based on the depth of fluid circulation in the basin. After reacting with different rocks, the fluids are enriched in Na, Ca, and Mg sulfates, and their salinity can increase tremendously.

Black shale: a fine-grained clastic sedimentary mudrock composed of clay mineral flakes and other fragments, mainly quartz and calcite.

Breccia: a rock composed of broken fragments of minerals or rock cemented together by a fine-grained matrix.

Burgers vectors: a quantity, usually represented by an arrow, describing the magnitude and the direction of the lattice distortion resulting from a dislocation.

Cataclasite: a rock consisting of angular *clasts* in a fine-grained matrix that formed by fracturing and pulverization of the rock during faulting.

Clast: a fragment of pre-existing mineral or rock.

Coquina limestone: slightly cemented sedimentary rock formed almost completely of sorted fossils, generally shell and shell fragments.

Daughter mineral: the new phases formed in a fluid inclusion cavity that have precipitated from the solution within.

Décollement plane: a low-angle dipping fault or shear zone corresponding to a gliding plane between two rock masses. These planes are developed in compressional tectonic settings (involving folding and overthrusting) and extensional settings. Also known as a basal detachment fault.

Dendrite: A portion of the trapiche texture having sawtooth contact with the core and the arms and formed by dendritic growth (i.e., a high degree of supersaturation, see box B). In agreement with the literature, the word can also be used to refer to feather-edge morphologies due to the incorporation of matrix material (as in this study).

Detachment: see *décollement plane*

Diffraction vector g: In a crystal of any structure, vector **g** is normal to the planes (*hkl*) and has a length inversely proportional to the distance between the planes.

Dolomitic limestone (or dolomite): an anhydrous carbonate mineral with the formula (Ca, Mg)$(CO_3)_2$.

Drag folds: curvature that represents the bending of rocks before they break. Drag folds occur in conjunction with faults.

Drusy cavity: a hollow space within a rock with a crust of tiny crystals.

En echelon vein: also known as *tension gash* arrays, these veins are characteristic of ductile-brittle shear zones. They are sets of short, parallel planar lenses on the surface of a rock. En echelon veins originate as tension fractures and are subsequently filled through the precipitation of a mineral, most commonly calcite or quartz.

Eutectic system: a mixture of two species that melt and solidify at constant temperature. The eutectic system behaves in fact as a pure body from the standpoint of fusion.

Evaporites: any sedimentary rock such as gypsum, anhydrite, or rock salt (such as halite or sylvite) that is formed by precipitation from evaporating seawater.

Extensional vein: equivalent of *tension gash*.

Fluidization phenomena: transport of rock fragments and breccia by a fluid (liquid or gas) in a fault structure. During fluid flow, the heavier fragments of the breccia are transported, suspended, rotated, sorted, and cemented by the matrix. The fragments and matrix are suspended and transported as a fluid-supported pulp.

Framboidal: Referring to a texture of roughly spherical aggregates of discrete rounded equi-angular euhedral microcrystallites approximately 0.5 µm in diameter, with an average aggregate size ranging from 5 to 20 µm.

Hydraulic breccia: a rock formation resulting from hydraulic fracturing, in which the hydrostatic pressure is greater than lithostatic pressure. Hydraulic fracturing may create a *breccia* that is filled with vein material. Such vein systems may be quite extensive, and can form in the shape of tabular dipping sheets, diatremes, or laterally extensive mantos controlled by boundaries such as *thrust* faults, competent sedimentary layers, or cap rocks.

Incremental thrust propagation: the propagation of a dislocated part of the terrane over an area in relatively small overlapping increments.

Internal over- and underpressure: When trapped by a mineral, pressure and temperature conditions preserved by fluid inclusion cavities can sometimes suffer re-equilibration during growth. As a result, the cavities can suffer internal overpressure when the internal pressure in the inclusion exceeds the external confining pressure, or internal underpressure when the internal pressure is lower than the external confining pressure.

Jogs (or bends): a gap or segment between two fault plane with the same strike and slip direction. Jogs offset perpendicular to the slip direction.

Klippe: in *thrust fault* terrains, the remnant of a nappe after erosion has removed the connecting portions.

Layer-by-layer growth: a growth mechanism based on two-dimensional nucleation.

Listric faults: faults in which the fault plane curves; the dip is steeper near the surface and shallower with increased depth.

Lithostatic pressure: the pressure or stress imposed on a layer of soil or rock by the weight of material. It is also called overburden pressure, confining pressure, or vertical stress.

Metasomatism: the chemical alteration of a rock by hydrothermal and/or other fluids. The chemical elements of the mother rock undergo fluid transport, accompanied by a modification (metasomatic process) of chemical composition to form a daughter rock.

Meteoric water: the water derived from precipitation that forms ice melts and bodies of water such as rivers and lakes.

Mohr's circle: A diagram that graphically illustrates in two dimensions the complex relationships between components of normal and shear stress.

Nappe: a large sheetlike body that moved more than two kilometers above the thrust fault from its original location.

Necking-down: a re-equilibration process of the morphology of a fluid cavity during cooling. This post-entrapment phenomenon changes the shape of the cavity by splitting it into smaller fluid inclusions. Necking-down leads to a distribution of the phases (vapor, liquid, solid) that is different from the original fluid inclusion assemblage.

Olistostrome: a sedimentary deposit composed of a chaotic mass of heterogeneous material, such as blocks and mud. The mass accumulates as a semi-fluid body via submarine gravity sliding or slumping of the loose materials.

Overthrusting: large total displacement of *thrust faults*.

Phyllosilicates: silicate minerals with sheet-like structures.

Pinacoidal faces: two equivalent faces related by an inversion center.

Scalar product: the product of the magnitudes of two vectors and the cosines of the angles between them.

Shear zone: a zone of strong deformation with a high strain rate surrounded by rocks with a lower state of finite strain. It is characterized by a length-to-width ratio of more than 5:1. Shear zones form a continuum of geological structures, ranging from brittle to brittle-ductile (or semi-brittle), ductile-brittle, and ductile shear zones.

Space group: A set of symmetry operations of a three-dimensional crystal pattern.

Stringers: oblique growth of emeralds at 60° to each other occurring in the dendrites. They are also observed in other trapiche minerals such as chiastolite and garnet, where they form at 90° and 60°, respectively (Rice, 1993).

Subsiding marine basin: areas generally characterized by thick accumulation of marine sediments. Subsidence is controlled by tectonic (e.g. normal faults as in passive margin or rift basin) and thermal re-equilibration of thinned crust.

Supersaturation (or undercooling): the difference between the concentration C_∞ at the equilibrium temperature T_E of a saturated solution and the concentration C at the growth temperature T_G (Sunagawa, 2005). Supersaturation is critical because it is the driving force for crystal nucleation and growth.

Tear faults: small-scale local strike-slip faults. Strike-slip faults with left-lateral motion are known as sinistral faults, those with right-lateral motion are known as dextral faults. Each is defined by the direction of movement of the ground on the opposite side of the fault from an observer. Tear faults are associated with other structures such as folds, thrust faults, and normal faults. In a thrust belt, the tear faults strike perpendicular to the thrust front and fold axis. As the thrust sheet propagates into the foreland, the tear faults start to segment the thrust sheets, eventually acting as lateral boundaries that separate the thrust units.

Tension gash: veins characteristic of ductile-brittle shear zones, classically disposed en echelon when non-coaxial strain is applied to rocks (see *en echelon vein*). Also called *extensional veins*.

Thermal reduction of sulfate: redox reactions in which sulfate is reduced by hydrocarbons, either bacterially (bacterial sulfate reduction) or inorganically (thermochemical sulfate reduction).

Thrust fault: a fault with a very low dip angle and a very large total displacement of the terranes, called *overthrust* or detachment. Thrust faults are characteristic of compressive tectonics. This process results in an outlier of exotic, often nearly horizontally translated strata called "nappe" overlying autochthonous strata.

Undulatory extinction: the consequence of tectonic constraints, seen as a darker zone during the rotation of the microscope stage. Also called wavy extinction.

REFERENCES

Agrosì G., Bosi F., Lucchesi S., Melchiorre G., Scandale E. (2006) Mn-tourmaline from island of Elba (Italy): Growth history and growth marks. *American Mineralogist*, Vol. 91, Nos. 5–6, pp. 944–952, http://dx.doi.org/10.2138/am.2006.1978

Agrosì G., Tempesta G., Scandale E., Harris J. W. (2013) Growth and post-growth defects in a diamond from Finsch mine (South Africa). *European Journal of Mineralogy*, Vol. 25, No. 4, pp. 551–559, http://dx.doi.org/10.1127/0935-1221/2013/0025-2301

Andersen T.B. (1984) Inclusion patterns in zoned garnet from Magerøy, north Norway. *Mineralogical Magazine*, Vol. 48, No. 346, pp. 21–26, http://dx.doi.org/10.1180/minmag.1984.048.346.03

Andrianjakavah P.R., Salvi S., Béziat D., Rakotondrazafy A.F.M., Giuliani G. (2009) Proximal and distal styles of pegmatite-related metasomatic emerald mineralization at Ianapera, southern Madagascar. *Mineralium Deposita*, Vol. 44, No. 7, pp. 817–835, http://dx.doi.org/10.1007/s00126-009-0243-5

Artioli G., Rinaldi R., Ståhl K. (1993) Structure refinements of beryl by single-crystal neutron and X-ray diffraction. *American Mineralogist*, Vol. 78, pp. 762–768.

Atherton M.P., Brenchley P.J. (1972) A preliminary study of the structure, stratigraphy and metamorphism of some contact rocks of the Western Andes, near the Quebrada Venado Muerto, Peru. *Geological Journal*, Vol. 8, pp. 161–178, http://dx.doi.org/10.1002/gj.3350080114

Aurisicchio C., Fioravanti G., Grubessi O., Zanazzi P.F. (1988) Reappraisal of the crystal chemistry of beryl. *American Mineralogist*, Vol. 73, Nos. 7–8, pp. 826–837.

Authier A., Zarka A. (1994) X-ray topographic study of the real structure of minerals. In A.S. Marfunin, Ed., *Composition, Structure and Properties of Mineral Matter*, Springer-Verlag, Berlin, pp. 221–233.

Banks D.A., Giuliani G., Yardley B.W.D., Cheilletz A. (2000) Emerald mineralisation in Colombia: fluid chemistry and the role

of brine mixing. *Mineralium Deposita*, Vol. 35, No. 8, pp. 699–713, http://dx.doi.org/10.1007/s001260050273
Barriga Villalba A.M. (1948) Estudio cientifico de la Esmeraldas de Colombia. In *Esmeraldas de Colombia*, Banco de la Republica Publisher, Bogotá, Colombia Parte II, pp. 97–133 [in Spanish].
Befi R. (2012) Gem News International: Trapiche aquamarine from Namibia. *G&G*, Vol. 48, No. 2, pp. 143–144.
Berg W.F. (1938) Crystal growth from solutions. *Proceedings of the Royal Society*, Vol. 164, No. 916, pp. 79–95, http://dx.doi.org/10.1098/rspa.1938.0006
Bergt W. (1899) Die älteren Massengesteine, kristalli nen Schiefer und Sedimente, p. 46. In F. Bernauer Ed., *Compilación de los Estudios Geológicos Oficiales en Colombia -1917 a 1933*, No. 4, pp. 199–221 (in German).
Bernauer F., Ed. (1933) Las llamadas maclas multiples de esmeralda de Muzo y sus anomalias opticas. *Compilación de los Estudios Geológicos Oficiales en Colombia -1917 a 1933*, No. 4, pp. 199–221 (in Spanish).
Bertrand E. (1879) Compte-rendu de la séance du 13 Février 1879 [Report of the meeting of February 13, 1879]. *Bulletin de la Société Minéralogique de France*, Vol. 2, p. 31.
Beus A.A. (1979) Sodium - a geochemical indicator of emerald mineralization in the Cordillera oriental, Colombia. *Journal of Geochemical Exploration*, Vol. 11, No. 2, pp. 195–208, http://dx.doi.org/10.1016/0375-6742(79)90023-2
Beus A.A., Mineev D.A. (1972) *Some geological and geochemical features of the Muzo and Coscuez emerald zone, Cordillera oriental, Colombia.* INGEOMINAS, Informe 1689, 50 pp.
Branquet Y. (1999) Etude structurale et métallogénique des gisements d'émeraude de Colombie: contribution à l'histoire tectono-sédimentaire de la cordillère orientale de Colombie. PhD Thesis, Université de Lorraine, Nancy, France [in French].
Branquet Y. Laumonier B., Cheilletz A., Giuliani G. (1999a) Emeralds in the eastern Cordillera of Colombia: two tectonic settings for one mineralisation. *Geology*, Vol. 27, No. 7, pp. 597–600, http://dx.doi.org/10.1130/0091-7613(1999)027%3C0597:EITECO%3E2.3.CO;2
Branquet Y., Cheilletz A., Giuliani G., Laumonier B., Blanco O. (1999b) Fluidized hydrothermal breccia in dilatant faults during thrusting: The Colombian emerald deposits. In *Fractures, Fluid and Mineralization*. Geological Society, London, 1999, Special Publication 155, pp. 183–195.
Branquet Y., Giuliani G., Cheilletz A., Laumonier B. (2015) Colombian emeralds and evaporites: tectono-stratigraphic significance of a regional emerald-bearing evaporitic breccia level. *13th SGA Biennial Meeting*, Nancy, France, Proceedings Vol. 4, pp. 1291–1294.
Breeding C.M., Shen A.H., Eaton-Magaña S., Rossman G.R., Shigley J.E., Gilbertson A. (2010) Developments in gemstone analysis techniques and instrumentation during the 2000s. *G&G*, Vol. 46, No. 3, pp. 241–257, http://dx.doi.org/10.5741/GEMS.46.3.241
Bryan W.B. (1972) Morphology of quench crystals in submarine basalts. *Journal of Geophysical Research*, Vol. 77, No. 29, pp. 5812–5819, http://dx.doi.org/10.1029/JB077i029p05812
Burton K.W. (1986) Garnet-quartz intergrowths in graphitic pelites: the roles of the fluid phase. *Mineralogical Magazine*, Vol. 50, pp. 611–620, http://dx.doi.org/10.1180/minmag.1986.050.358.06
Byerly G.R., Palmer M.R. (1991) Tourmaline mineralization in the Barberton greenstone belt, South Africa: early Archean metasomatism by evaporite-derived boron. *Contributions to Mineralogy and Petrology*, Vol. 107, No. 3, pp. 387–402, http://dx.doi.org/10.1007/BF00325106
Carstens H. (1986) Displacive growth of authigenic pyrite. *Journal of Sedimentary Petrology*, Vol. 56, No. 2, pp. 252–257.
Charoy B. (1998) Cristallochimie du béryl: l'état des connaissances. In *L'émeraude*, Association Française de Gemmologie-CNRS-ORSTOM, Groupe Rosay, Paris, France, pp. 47–54 (in French).
Chaudhari M.W. (1969) An unusual emerald. *Schweizerische Mineralogische und Petrographische Mitteilungen*, Vol. 49, No. 3, pp. 569–575.
Cheilletz A., Giuliani G. (1996) The genesis of Colombian emeralds: a restatement. *Mineralium Deposita*, Vol. 31, No. 5, pp. 359–364, http://dx.doi.org/10.1007/BF00189183
Cheilletz A., Féraud G., Giuliani G., Rodriguez C.T. (1994) Time-pressure and temperature constraints on the formation of Colombian emeralds; an $^{40}Ar/^{39}Ar$ laser microprobe and fluid inclusion study. *Economic Geology*, Vol. 89, No. 2, pp. 362–380, http://dx.doi.org/10.1180/10.2113/gsecongeo.89.2.361
Cheilletz A., Giuliani G., Branquet Y., Laumonier B., Sanchez A.J., Féraud G., Arthan T. (1997) Datation K-Ar et $^{40}Ar/^{39}Ar$ à 65 ± 3 Ma des gisements d'émeraude du district de Chivor-Macanal: argument en faveur d'une déformation précoce dans la Cordillère Orientale de Colombie. *Comptes Rendus de l'Académie des Sciences*, Paris, Sér. IIa, Vol. 324, pp. 369–377 (in French).
Cnudde V., Boone M.N. (2013) High-resolution X-ray computed tomography in geosciences: a review of the current technology and applications. *Earth-Science Reviews*, Vol. 123, pp. 1–17, http://dx.doi.org/10.1016/j.earscirev.2013.04.003
Codazzi R.L. (1915) Los minerales de Muzo. *Contribución al Estudio de los Minerales de Colombia*, Bogotá, pp. 3–7 (In Spanish).
Damon P.E., Kulp J.L. (1958) Excess helium and argon in beryl and other minerals. *American Mineralogist*, Vol. 43, Nos. 5–6, pp. 433–459.
DelRe N. (1994) Lab Notes: Emerald, trapiche from a new locality. *G&G*, Vol. 30, No. 2, pp. 116–117.
Faure F., Trolliard G., Nicollet C., Montel J.M. (2003) A development model of olivine morphology as a function of the cooling rate and the degree of undercooling. *Contributions to Mineralogy and Petrology*, Vol. 145, No. 2, pp. 251–263, http://dx.doi.org/10.1007/s00410-003-0449-y
Faure F., Schiano P., Trolliard G., Nicollet C., Soulestin B. (2007) Textural evolution of polyhedral olivine experiencing rapid cooling rates. *Contributions to Mineralogy and Petrology*, Vol. 153, No. 4, pp. 369–492, http://dx.doi.org/10.1007/s00410-006-0154-8
Garnier V., Ohnenstetter D., Giuliani G., Blanc P., Schwarz D. (2002a) Trace-element contents and cathodoluminescence of "trapiche" rubies from Mong Hsu, Myanmar (Burma): geological significance. *Mineralogy and Petrology*, Vol. 76, Nos. 3–4, pp. 179–193, http://dx.doi.org/10.1007/s007100200040
Garnier V., Ohnenstetter D., Giuliani G., Schwarz D. (2002b) Rubis trapiches de Mong Hsu, Myanmar. *Revue de Gemmologie AFG*, Vol. 144, pp. 5–12 (in French).
Geake J.E., Walker G. (1975) *Luminescence of Minerals in the Near Infrared and Raman Spectroscopy of Lunar and Terrestrial Minerals*. Academic Press, New York, pp. 73–89.
Giuliani G., Rodriguez C.T., Rueda F. (1990) Les gisements d'émeraude de la Cordillère Orientale de la Colombie: nouvelles données métallogénies. *Mineralium Deposita*, Vol. 25, pp. 105–111 (in French).
Giuliani G., Cheilletz A., Dubessy J., Rodriguez C.T. (1991) H_2O-NaCl-$CaCl_2$-bearing fluids in emeralds from the Vega San Juan mine, Gachalá district, Colombia. *Plinius*, No. 5, p. 90.
Giuliani G., Sheppard S.M.F., Cheilletz A., Rodriguez C.T. (1992) Fluid inclusions and $^{18}O/^{16}O$, $^{13}C/^{12}C$ isotope geochemistry: contribution to the genesis of emerald deposits from the Oriental Cordillera of Colombia. *Comptes Rendus de l'Académie des Sciences*, Paris, Vol. 314, pp. 269–274.
Giuliani G., Cheilletz A., Dubessy J., Rodriguez C.T. (1993) Emerald deposits from Colombia: chemical composition of fluid inclusions and origin. *Proceedings of the 8th IAGOD Symposium*, Ottawa, pp. 159–168.
Giuliani G., Cheilletz A., Arboleda C., Carrillo V., Rueda F., Baker J. (1995) An evaporitic origin of the parent brines of Colombian emeralds: fluid inclusion and sulphur isotope evidence. *European Journal of Mineralogy*, Vol. 7, pp. 151–165.

Giuliani G., France-Lanord C., Zimmermann J-L., Cheilletz A. (1997) Fluid composition, δD of channel H_2O, and $\delta^{18}O$ of lattice oxygen in beryls: Genetic implications for Brazilian, Colombian, and Afghanistani emerald deposits. *International Geology Review*, Vol. 39, No. 5, pp. 400–424, http://dx.doi.org/10.1080/00206819709465280

Giuliani G., France-Lanord C., Cheilletz A., Coget P., Branquet Y., Laumonier B. (2000) Sulfate reduction by organic matter in Colombian emerald deposits: chemical and stable isotope (C, O, H) evidence. *Economic Geology*, Vol. 95, No. 5, pp. 1129–1153, tp://dx.doi.org/10.2113/95.5.1129

Giuliani G., Jarnot M., Neumeier G., Ottaway T., Sinkankas J., Staebler G. (2002) *Emeralds of the World*. ExtraLapis English No. 2: The Legendary green beryl. Lapis International Publisher, LLC, East Hampton, CT.

Giuliani G., Marty B., Banks D. (2005) Noble gases in fluid inclusions from emeralds: Implications for the origins of fluids and constraints on fluid-rock interactions. Abstract, *18th Biennial Meeting of European Current Research on Fluid Inclusions*, Siena, Italy, CD-ROM.

Götze J., Krbetschek M.R., Habermann D., Wolf D. (2000) High-resolution cathodoluminescence studies of feldspar minerals. In *Cathodoluminescence in Geosciences*. Springer Verlag, Berlin, pp. 245–270.

Groat L., Giuliani G., Marshall D., Turner D. (2014) Emerald. In *Geology of Gem Deposits*, Mineralogical Association of Canada, Short Course Series 44, Tucson, pp. 135–174.

Hainschwang T., Notari F., Anckar B. (2007) Trapiche tourmaline from Zambia. *G&G*, Vol. 43, No. 1, pp. 36–46, http://dx.doi.org/10.5741/GEMS.43.1.36

Hall M. (1993) Mineralogía y geoquímica de las vetas esmeraldíferas de Muzo, Departamento de Boyacá con implicaciones en la prospección futura de esmeraldas en otras partes de Colombia. *Compilación de los estudios geológicos oficiales en Colombia*. Tomo XIII, pp. 1–326 (In Spanish).

Harker A. (1950) *Metamorphic Textures*. Methuen and Co., London.

Hochleitner R. (2002) The emerald: mineralogically a beryl! In *Emeralds of the World,* ExtraLapis English No. 2: The Legendary green beryl. Lapis International, LLC, East Hampton, CT, pp. 11–17.

Hsu T. (2013) Gem News International: Rare double-trapiche emerald. *G&G*, Vol. 49, No. 1, p. 53.

Invernizzi C., Vityk M., Cello G., Bodnar R. (1998) Fluid inclusions in high pressure/low temperature rocks from the Calabrian Arc (Southern Italy): the burial and exhumation history of the subduction-related Diamante-Terranova unit. *Journal of Metamorphic Geology*, Vol. 16, No. 2, pp. 247–258, http://dx.doi.org/10.1111/j.1525-1314.1998.00138.x

Jia L.C., Chen M., Jin Y. (2014) 3D imaging of fractures in carbonate rocks using X-ray computed tomography technology. *Carbonates and Evaporites*, Vol. 29, No. 2, pp. 147–153.

Johnson M.L., Koivula J.I., Eds. (1998) Gem News: Beryl from Madagascar…and trapiche beryl. *G&G*, Vol. 34, No. 2, pp. 137–138.

Khotchanin K., Thanasuthipitak P., Thanasuthipitak T. (2010) Characteristics of trapiche blue sapphire from Southern Vietnam. *Chiang Mai Journal of Science*, Vol. 37, No. 1, pp. 64–73.

Kiefert L. (2012) Gem News International: Unusual trapiche sapphire. *G&G*, Vol. 48, No. 3, p. 229.

Koivula J.I. (2008) Gem News International: Two unusual aquamarines. *G&G*, Vol. 44, No. 3, pp. 275–276.

Koivula J.I., Kammerling R.C., Fritsch E., Eds. (1994) Gem News: "Trapiche" purple-pink sapphire. *G&G*, Vol. 30, No. 3, p. 197.

Kozlowski A., Metz P., Jaramillo H.A.E. (1988) Emeralds from Somondoco, Colombia: chemical composition, fluid inclusion and origin. *Neues Jahrbuch für Mineralogie Abhandlungen*, Vol. 59, pp. 23–49.

Lang A.R. (1959) The projection topograph: a new method in X-ray diffraction microradiography. *Acta Crystallographica*, Vol. 12, No. 3, pp. 249–250, doi:10.1107/S0365110X59000706.

Laumonier B., Branquet Y., Cheilletz A., Giuliani G., Rueda F. (1996) Mise en évidence d'une tectonique compressive Eocène-Oligocène dans l'Ouest de la Cordillère orientale de Colombie, d'après la structure en duplex des gisements d'émeraude de Muzo et Coscuez. *Comptes Rendus de l'Académie des Sciences, Paris, Série IIa*, Vol. 323, pp. 705–712 (in French).

Leiper H. (1967) Rare trapiche emerald crystals show unique twinning evidence. *Lapidary Journal*, Vol. 21, No. 4, pp. 565.

London D. (2008) *Pegmatites*. The Canadian Mineralogist, special publication No. 10, Mineralogical Association of Canada, Québec.

Lyckberg P. (2005a) Le béryl héliodore de Karélie (Finlande). *Le Règne Minéral*, Vol. 62, pp. 33–39 [in French].

——— (2005b) Gem beryl from Russia and Ukraine. In *Beryl and Its Color Varieties*, Lapis International Publishing, East Hampton, CT, pp. 49–57.

Mantilla Figueroa L.C., Silva A., Serrano J., Gomez J., Ramirez J., Meza J., Pelayo Y., Ortega L., Plata L., Peña E. (2007) *Investagación petrográfica y geoquímica de las sedimentitas del Cretácico inferior (K1) y sus manifestaciones hidrotermales asociadas; Planchas 169, 170, 189, 190 (Cordillera oriental): imlicacions en la búsqueda de Esmeraldas*. INGEOMINAS informe, Bogotá, Colombia, 330 pp. (In Spanish).

Maya M., Buenaventura J., Salinas R. (2004) *Estado del conocimiento de la exploracion de Esmeraldas en Colombia*. INGEOMINAS informe, Bogotá, Colombia, 89 pp. (In Spanish).

McKague H.L. (1964) Trapiche emeralds from Colombia. *G&G*, Vol. 11, No. 7, pp. 210–223.

Müllenmeister H.J., Zang J. (1995) Ein Trapiche-Rubin aus Myanmar (Burma). *Lapis*, Vol. 20, No. 12, p. 50 (in German).

Nassau K., Jackson K.A. (1970) Trapiche emeralds from Chivor and Muzo, Colombia. *American Mineralogist*, Vol. 55, Nos. 3–4, pp. 416–427.

O'Donoghue M.J. (1971) Trapiche emerald. *The Journal of Gemmology*, Vol. 12, No. 8, pp. 329–332.

Ohnenstetter D., Giuliani G., Bustos O. (1998) Emeraudes trapiches colombiennes. In *L'émeraude*. Connaissances actuelles et prospective. Association Française de Gemmologie, pp. 119–124 (in French).

Oppenheim V. (1948) The Muzo emerald zone, Colombia. *Economic Geology*, Vol. 43, No. 1, pp. 31–38, http://dx.doi.org/10.2113/gsecongeo.43.1.31

Ottaway T.L. (1991) The geochemistry of the Muzo emerald deposit, Colombia. Master's thesis, University of Toronto, Canada.

Ottaway T.L., Wicks F.J., Bryndzia L.T., Kyser T.K., Spooner E.T.C. (1994) Formation of the Muzo hydrothermal emerald deposit in Colombia. *Nature*, Vol. 369, No. 6481, pp. 552–554, http://dx.doi.org/10.1038/369552a0

Pogue J.E. (1916) The emerald deposits of Muzo, Colombia. *Transactions of the American Institute of Mining Engineers*, Vol. 55, pp. 383–406.

Pouchou J.L., Pichoir F. (1991) Quantitative analysis of homogeneous or stratified microvolumes applying the model "PAP." In K.F.J. Heinrich and D.E. Newbury, Eds., *Electron Probe Quantitation*, Springer Science-Business Media, New York, pp. 31–76.

Rakovan J., Kitamura M., Tumada O. (2006). Sakura ishi (cherry blossom stones): Mica pseudomorphs of complex cordierite-indialite intergrowths from Kameoka, Kyoto Prefecture, Japan. *Rocks and Minerals*, Vol. 81, No. 4, pp. 284–292, http://dx.doi.org/10.3200/RMIN.81.4.284-292

Rice A.H.N. (1993) Textural and twin sector-zoning and displacement of graphite in chiastolite and -pyralspite and grandite garnets in the variscides of South-West England. *Read at the Annual Conference of the Ussher Society*, pp. 129–131.

——— (2007) Chemical disequilibrium during garnet growth: Monte Carlo simulations of natural morphologies: Comment. *Geology*, Vol. 35, No. 1, pp. 124–125, http://dx.doi.org/10.1130/G23441C.1

Rice A.H.N., Mitchell J.I. (1991) Porphyroblast textural sector-zoning and matrix displacement. *Mineralogical Magazine*, Vol. 55,

No. 380, pp. 379–396, http://dx.doi.org/10.1180/minmag.1991.055.380.08
Ringsrud R. (2013) *Emeralds: A Passionate Guide*. GVP Publishing, Oxnard, CA.
Rodríguez E.M., Ulloa C.M. (1994) *Plancha 189-La Palma, Bogotá*, Ingeominas, scale 1:1000000.
Roedder E. (1963) Studies of fluid inclusions II: freezing data and their interpretation. *Economic Geology*, Vol. 58, No. 2, pp. 163–211, http://dx.doi.org/10.2113/gsecongeo.58.2.167
Roedder E. (1984) *Fluid Inclusions*. Mineralogical Society of America. Reviews in Mineralogy, Vol. 12, BookCrafters Publisher, Chelsea, MI.
Rondeau B., Fritsch E., Peucat J.-J., Nordrum F.S., Groat L. (2008) Characterization of emeralds from a historical deposit: Byrud (Eidsvoll), Norway. *G&G*, Vol. 44, No. 2, pp. 108–122, http://dx.doi.org/10.5741/GEMS.44.2.108
Scandale E., Zarka A. (1982) Sur l'origine des canaux dans les cristaux. *Journal of Applied Crystallography*, Vol. 15, No. 4, pp. 417–422, http://dx.doi.org/10.1107/S0021889882012291.
Scheibe R. (1926) Die Smaragdlagerstätte von Muzo (Kolombien) und ihre nähere Umberbung. *Neues Jahrbuch für Mineralogie Abhandlungen*, Vol. 54, pp. 419–447 (in German).
Scheibe R. (1933) Informe geológico sobre la mina de esmeraldas de Muzo. *Compilación de los Estudios Geológicos Oficiales en Colombia*, No. 1, pp. 169–198 (in Spanish).
Schiffman C.A. (1968) Unusual emeralds. *Journal of Gemmology*, Vol. 11, No. 4, pp. 105–114.
Schmetzer K., Hänni H.A., Bernhardt H.J., Schwarz D. (1996) Trapiche rubies. *G&G*, Vol. 32, No. 4, pp. 242–250, http://dx.doi.org/10.5741/GEMS.32.4.242
Schmetzer K., Beili Z., Yan G., Bernhardt H.J., Hänni H.A. (1998) Element mapping of trapiche rubies. *Journal of Gemmology*, Vol. 26, No. 5, pp. 289–301.
Schmetzer K., Bernhardt H.J., Hainschwang T. (2011) Chemical and growth zoning in trapiche tourmaline from Zambia – a re-evolution. *Journal of Gemmology*, Vol. 32, No. 5-8, pp. 151–173.
Schwarz D., Schmetzer, K. (2002) The definition of emerald: the green variety of beryl colored by chromium and/or vanadium. In *Emeralds of the World*, ExtraLapis English No. 2: The Legendary green beryl. Lapis International, LLC, East Hampton, CT, pp. 74–78.
Sunagawa I. (1987) Morphology of minerals. In I. Sunagawa, Ed., *Morphology of Crystals, Part B*. Terra Scientific Publishing Company, Tokyo, pp. 509–587.
Sunagawa I. (1999) Growth and morphology of crystals. *Forma*, Vol. 14, pp. 147–166.
Sunagawa I. (2005) *Crystals: Growth, Morphology and Perfection*. Cambridge University Press, Cambridge, UK.
Sunagawa I., Bernhardt H.J., Schmetzer K. (1999) Texture formation and element partitioning in trapiche ruby. *Journal of Crystal Growth*, Vol. 206, No. 4, pp. 322–330, http://dx.doi.org/10.1016/S0022-0248(99)00331-0
Tempesta G., Scandale E., Agrosì G. (2011) Striations and hollow channels in rounded beryl crystals. *Periodico di Mineralogia*, Vol. 79, No.1, pp. 75–87.
Touray J.C., Poirot J.P. (1968) Observations sur les inclusions fluides primaires de l'émeraude et leurs relations avec les inclusions solides. *Comptes Rendus de l'Académie des Sciences*, Paris, Sér. D, Vol. 266, pp. 305–308 (in French).
Tripp E.J., Hernandez L.H. (1970) The complete trapiche emerald picture. The cutting of gems from trapiche crystals. *Lapidary Journal*, Vol. 24, No. 1, pp. 97–104.
Tsuchiyama A., Uesugi K., Nakano T., Ikeda S. (2005) Quantitative evaluation of attenuation contrast of X-ray computed tomography images using monochromatized beams. *American Mineralogist*, Vol. 90, No. 1, pp. 132–142, http://dx.doi.org/10.2138/am.2005.1552
Ulloa C. (1980) Ambiente geológico de los yacimientos esmeraldíferos en Colombia. *Boletin Sociedad Geológica Perú*, Vol. 65, pp. 157–170.
Vuillet P., Giuliani G., Fischer J.C., Chiappero P.J. (2002) Emeraudes de Gachala, Colombie: historique, genèse et découvertes paléontologiques. *Le Règne Minéral*, No. 46, pp. 5–18 (in French).
Ward F. (1993) *Emeralds*. Gem Book Publishers, Bethesda, MD.
White W.B., Masako M., Linnehan D.G., Furukawa T., Chandrasekhar B.K. (1986) Absorption and luminescence of Fe^{3+} in single-crystal orthoclase. *American Mineralogist*, Vol. 71, Nos. 11–12, pp. 1415–1419.
Wilbur D.E., Ague J.J. (2006) Chemical disequilibrium during garnet growth: Monte Carlo simulations of natural crystal morphologies. *Geology*, Vol. 34, No. 8, pp. 689–692, http://dx.doi.org/10.1130/G22483.1
Win K.K. (2005) Trapiche of Myanmar. *Australian Gemmologist*, Vol. 22, No. 6, pp. 269–270.
Wood D.L., Nassau K. (1968) Characterization of beryl and emerald by visible and infrared absorption spectroscopy. *American Mineralogist*, Vol. 53, Nos. 5–6, pp. 777–800.
Yardley B.W.D. (1974) Porphyroblasts and "crystallization force": Discussion of some theoretical considerations. *Geological Society of America Bulletin*, Vol. 85, No. 1, pp. 61–62, http://dx.doi.org/10.1130/0016-7606(1974)85<61:PACFDO>2.0.CO;2
Zwaan J.C., Jacob D.E., Häger T., Cavalcanti Neto M.T.O., Kanis J. (2012) Emeralds from the Fazenda Bonfim region, Rio Grande do Norte, Brazil. *G&G*, Vol. 48, No. 1, pp. 2–17, http://dx.doi.org/10.5741/GEMS.48.1.2